



Computational modeling and analysis of flow-induced vibration of an elastic splitter plate using a sharp-interface immersed boundary method

Anup Kundu¹ · Atul K. Soti² · Hemanshul Garg³ · Rajneesh Bhardwaj³ · Mark C. Thompson⁴

Received: 7 November 2019 / Accepted: 6 May 2020 / Published online: 22 May 2020
© Springer Nature Switzerland AG 2020

Abstract

We present the development and benchmarking of an in-house fluid–structure interaction (FSI) solver. An implicit partitioned approach is utilized to couple a sharp-interface immersed boundary method-based flow solver and a finite-element method-based structural solver. In the present work, the coupling is accelerated using a dynamic under-relaxation scheme. The revised coupling is around two to three times faster and numerically stable, as compared to the one that uses a constant under-relaxation parameter. The solver is validated against two FSI benchmarks in which a thin, finite thickness, elastic splitter plate is attached to the lee side of a circular or square rigid cylinder, subjected to laminar flow. In these two-dimensional benchmarks, the flow induces a wave-like deformation in the plate, and it attains a periodic self-sustained oscillation. We employ the FSI solver to analyze the flow-induced vibration (FIV) of the plate in a uniform laminar free-stream flow for a wide range of mass ratio and bending stiffness at Reynolds number (Re) of 100, based on the diameter of the cylinder. At the given Re , two-dimensional numerical simulations show that the FIV of the plate effectively depends only on the mass ratio and bending stiffness. The largest displacement of the plate vibration is found to occur in the lock-in region, where the vortex shedding frequency of the coupled fluid–structure system is close to the natural frequency of the splitter plate. We briefly discuss wake structures and phase plots for different cases of mass ratio and bending stiffness.

Keywords Fluid–structure interaction (FSI) · Flow-induced vibration (FIV) · Immersed boundary (IB) method

1 Introduction

Flow-induced vibration (FIV) of an elastic plate subjected to laminar flow has potential applications in energy harvesting [1, 2] and thermal augmentation [3–5]. The interaction of fluid flow with a flexible structure may lead to large-scale FIV due to the resonant forcing of the structure caused by periodic vortex shedding. Fluid–structure interaction (FSI) modeling of large-scale FIV poses a significant challenge of tackling a deforming structure in a fluid

domain. Moreover, geometric and/or material nonlinearity should be accounted for in the structural solver. The nonlinear system of governing equations of the fluid and structure may be strongly coupled to accurately capture large-scale FIV. Such nonlinear FSI systems exhibit a large amplitude of FIV over a wide range of flow velocity [6], potentially useful in broadband energy harvesting devices.

Previous studies attempted the computational modeling of moving structure in a fluid domain using either immersed boundary (IB) method or arbitrary

✉ Rajneesh Bhardwaj, rajneesh.bhardwaj@iitb.ac.in | ¹C. V. Raman College of Engineering, Bhubaneswar 752054, India. ²Department of Mechanical Engineering, Indian Institute of Guwahati, Guwahati 781039, India. ³Department of Mechanical Engineering, Indian Institute of Technology Bombay, Mumbai 400076, India. ⁴Department of Mechanical and Aerospace Engineering, Monash University, Melbourne 3800, Australia.



Lagrangian–Eulerian (ALE) method. In the latter, a structure-conformal grid is used and it gets distorted at each time step due to flow-induced deformation (FID) of the structure. Therefore, a new mesh should be generated and the numerical solution should be mapped to this new grid. By contrast, the former is well suited to address this computational challenge as compared to the latter. A structure non-conformal (oftentimes a Cartesian) grid is used in the IB method, and there is no need to remesh the fluid domain while tackling a moving structure boundary. A review of variants of IB methods is provided by Mittal and Iaccarino [7] and Sotiropoulos and Yang [8].

In order to account structural dynamics in an FSI system, previous studies successfully integrated finite-element-based structural solver with existing flow solvers. For example, Bhardwaj and Mittal [9] proposed an FSI solver by coupling a sharp-interface IB method and an open-source finite-element solver (Tahoe), using an implicit partitioned approach. Employing this solver, they validated the FSI benchmark, proposed by Turek and Hron [10]. In this benchmark, an elastic plate attached to a rigid cylinder attains self-sustained oscillation in a laminar channel flow. Similarly, Tian et al. [11] proposed a versatile FSI solver which could handle large-scale FID of a flexible structure. They carried out several validations with established benchmarks and demonstrated the three-dimensional capability of the solver. Bailoor et al. [12] coupled a compressible flow solver with an open-source finite-element solver (Tahoe) to simulate blast loading on thin plates. Very recently, Furquan and Mittal [13] numerically studied two side-by-side flexible splitter plates attached to square cylinders using a deforming-spatial-domain/stabilized space–time flow solver coupled with a finite-element open-source structural dynamics solver.

The dynamic relaxation using Aitken's method was employed to accelerate the convergence of the coupling between the flow and structural solver in previous reports. Küttler and Wall [14] demonstrated a successful implementation of the dynamic relaxation using Aitken's method in an FSI solver based on the ALE method. They showed a reduction in the number of sub-iterations by two to four times as compared to the constant under-relaxation scheme. Similarly, Borazjani et al. [15] implemented Aitken's method in an IB method-based flow solver coupled with an elastically mounted rigid structure. Later, Kim et al. [16] reported the implementation of the Aitken's method for an IB method-based flow solver and a structural dynamics solver, coupled using weak and strong couplings. Degroote et al. [17] also presented a detailed algorithm that employed Aitken's method.

Several previous reports elucidated the flow physics of a rigid splitter plate mounted on a cylinder. Vu et al. [18] numerically examined the effects of splitter plate length

and Reynolds numbers on flow characteristics and drag/lift coefficients at $Re = 60 - 180$. They found that a critical plate length exists to suppress the vortex shedding. Sarioglu [19] measured flow field around a rigid splitter plate mounted on a square cylinder at $Re = 30,000$, keeping the plate length equal to cylinder diameter. The author varied the angle of incidence and reported a large Strouhal number and the lowest drag at an angle of 13° . Similarly, Chauhan et al. [20] experimentally measured the flow field around a rigid plate mounted on a square cylinder at $Re = 485$. They varied plate length from 0 to 6 times of the cylinder width and reported that a secondary vortex appears near the trailing edge of the plate for a threshold plate length.

Several previous studies [21–24] defined two important dimensionless parameters that govern the dynamics of a flexible plate subjected to fluid flow, namely the bending stiffness (K_b) and the mass ratio (M). These are given by

$$K_b = \frac{E^* h^{*3}}{\rho_f^* U_\infty^{*2} 12L^{*3}}, \quad (1)$$

$$M = \frac{\rho_p^* h^*}{\rho_f^* L^*}, \quad (2)$$

where the superscript * denotes a dimensional variable. Here, E^* , ρ_f^* , U_∞^* , h^* , L^* and ρ_p^* are the Young's modulus of the plate, fluid density, free-stream velocity, plate thickness, plate length and plate density, respectively. Note that K_b is defined per unit spanwise width of the plate in Eq. 1. Physically, K_b represents the ratio of restoring force produced by stiffness to the loading on the structure by the fluid. The parameter M represents the ratio of the density of the structure to that of the fluid, which is often referred to as the mass ratio. In addition, the reduced velocity U_R is another important parameter, defined as the ratio of the characteristic time scale of the structure to that of the fluid [25], and is given by,

$$U_R = \sqrt{\frac{M}{K_b}}. \quad (3)$$

The dynamics of thin, flexible plate oscillations subjected to a free-stream flow has been reported in several studies. Watanabe et al. [26] studied the flutter of a paper sheet using an analytical method and reported high flutter modes at low M . Argentina and Mahadevan [27] proposed a critical speed for the onset of flapping and estimated the flapping frequency based on scaling analysis. Tang and Paidoussis [25] investigated the dynamics of a flexible plate using an Euler–Bernoulli model coupled with an unsteady lumped vortex model. They investigated the flutter boundary and the post-critical behavior of this FSI

system. They obtained the flutter boundary in the form of the critical flow velocity versus the length of the flexible plate. They observed that the critical flow velocity is sensitive to short plate lengths.

Previous studies reported different regimes of flapping or flutter of a thin plate. A comprehensive review of such regimes was provided by Shelley and Zhang [28]. Connell and Yue [21] proposed a regime map of flag flutter based on their FSI simulations. They proposed the following three categories of plate dynamics: fixed-point stability, limit-cycle flapping and chaotic flapping. Fixed-point stability occurs when the flag aligns with the flow. As the flow velocity is increased, limit-cycle flapping takes over, characterized by single-frequency repeating flag oscillations. Chaotic flapping occurs as the flow velocity is further increased. Similarly, Lee et al. [29] examined the flapping dynamics of a flexible flag in a uniform flow. They found three different flapping states such as regular flapping, irregular flapping and irregular flapping with violent snapping by varying M and K_b .

Alben and Shelley [30] simulated the nonlinear dynamics of a flexible sheet in a 2D inviscid fluid. They characterized the behavior of flapping flags at large amplitudes and over many flapping periods and demonstrated a transition from a periodic to a chaotic flapping as the bending rigidity was decreased. They also found the stability boundary of the flow-aligned state for a flag within the two-dimensional parameter space of dimensionless flag inertia and bending rigidity. Employing a linear stability analysis, Connell and Yue [21] found the existence of a critical mass ratio for the chaotic flapping of the plate. Similarly, Eloy et al. [31] studied the linear stability of a flexible plate immersed in axial flow and found that a finite-span plate is stable than the infinite-span plate. Eloy et al. [32] addressed the linear stability of the rectangular plate in uniform flow and incompressible axial flow by varying aspect ratios. They identified critical velocities for the instability transitions as a function of system parameters, showing good agreement with their data.

Akabay and Young [23] examined the dynamic response and stability of piezoelectric beams in viscous and axial flows. They showed that a heavy beam undergoes flutter in a light fluid when the fluid inertial forces are in the balance with the solid elastic restoring forces, and for a light beam in a heavy fluid, flutter occurs when the fluid inertial force dominates the solid inertial force. Recently, Shoel and Mittal [3] numerically studied the dynamics of a self-oscillating reed in a channel flow, and they found that heavy reeds have higher critical velocities and have low oscillation frequencies and amplitudes. In a follow-up study, they predicted the flutter instability inside for a plate confined in a 2D channel of height H on the $M-U_r$ plane for a channel length $L = 1$, for $Re = 400$ [33].

They found that confinement induces a destabilizing effect and increases the oscillation frequency and compared the stability curves for different values of the H/L ratio. Their study found that using confinement and the asymmetric position of the plate could be used to adjust the flutter frequency and flutter instability.

In the context of an elastic splitter plate mounted on a rigid cylinder, Turek and Hron [10] proposed a FSI benchmark in which the elastic splitter plate of aspect ratio 17.5 attains a self-sustained periodic oscillation in a channel flow. Using the same configuration of Turek and Hron [10], Bhardwaj and Mittal [9] numerically showed that the oscillation frequency of the plate varies linearly with the dilatational wave speed inside the plate. Kundu et al. [34] showed that the computed plate frequency in the lock-in regime scales as the second mode of the natural frequency of a vibrating cantilevered plate (f_{ni}^*) in the vacuum. In this context, the natural frequency of an elastic plate fixed at one end is obtained using the Euler–Bernoulli beam model and is given by [34, 35],

$$f_{ni}^* = \frac{k_i^2}{2\pi} \sqrt{\frac{E^* I^*}{\rho_p^* A^* L^{*4}}}, \quad (4)$$

where $i = 1, 2, 3$ represents the frequency modes of the plate, $E^* I^*$ is the dimensional flexural rigidity of the beam and k_i are the respective constants for the modes. The values of k are 1.875, 4.694 and 7.855 for the first, second and third mode of the natural frequency, respectively. Also, ρ_p^* , A^* and L^* are the structure density, cross-sectional area and length of the plate, respectively. Using Eqs. 1 and 2, the non-dimensional form of Eq. 4 is expressed as follows:

$$f_{ni} = \frac{k_i^2}{2\pi L} \sqrt{\frac{K_b}{M}}. \quad (5)$$

Kundu et al. [34] also studied the effect of Reynolds number (Re) and length of the splitter plate on its flapping frequency. Shukla et al. [36] experimentally showed that the amplitude of the oscillation of a splitter plate attached to a circular cylinder increases with Re based on the cylinder diameter and they reported a plateau oscillation amplitude at $Re > 4000$. Very recently, Sahu et al. [37] numerically investigated the dynamics of an elastic splitter plate mounted on an elastically mounted cylinder.

The above literature survey shows that the FIV of the plate exhibits complex and coupled physics, and most of the previous investigations [21, 24, 29, 33, 38] neglected the thickness of the plate in the modeling and/or considered a membrane-like structure. For instance, the ratio of thickness to length, K_b and M was restricted to $O(0.01)$, $O(10^{-3})$ and $O(1)$, respectively, in the previous reports. In the context of the development

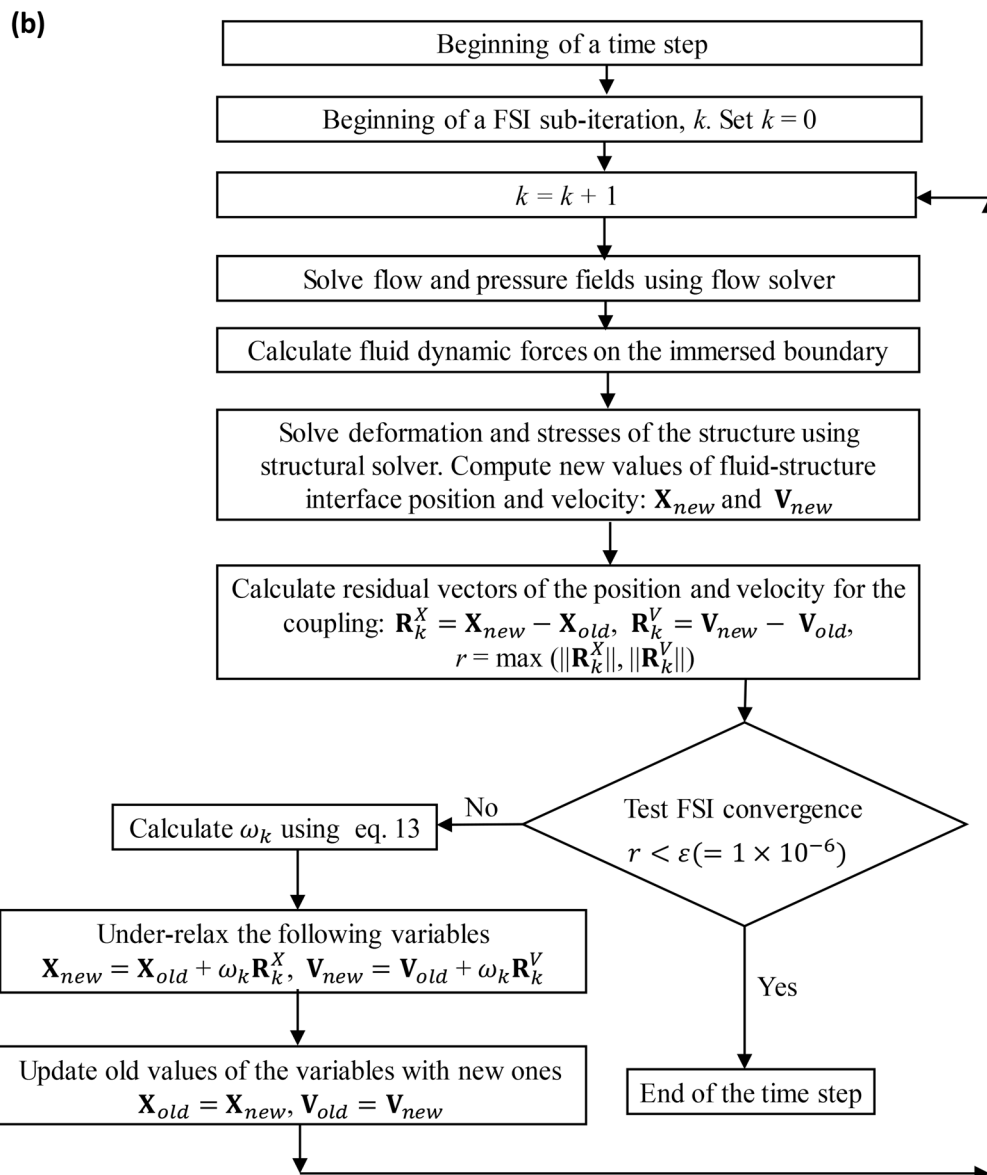
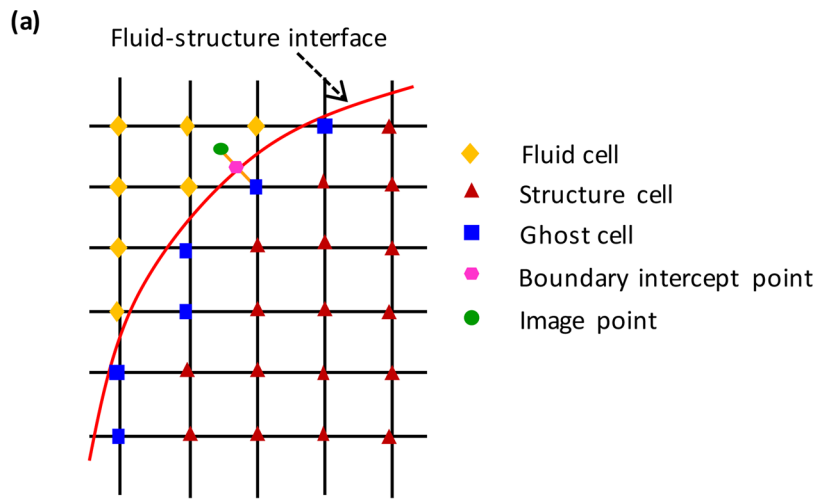


Fig. 1 **a** Schematic of the IB method proposed by Mittal et al. [39]. **b** Flowchart of the implicit coupling between flow and structural solver utilizing dynamic under-relaxation method for one time-step

of FSI solver, while previous studies successfully demonstrated the advantage of Aitken's method including those in IB-based solvers [14–17], an FSI solver with a strongly coupled high-fidelity structural solver and that can handle large-scale FID of the structure has not been reported thus far, to the best of our knowledge.

Therefore, to address these computational challenges and capture the coupled physics during FIV, the objective of the present study is twofold. The first is to develop and benchmark a high-fidelity FSI computational model that can tackle the large-scale FID of a thin structure. In particular, the implicit (strong) coupling between an in-house sharp-interface IB method-based flow solver and an open-source, finite-element-based structural dynamics solver is significantly accelerated using a dynamic under-relaxation method in the present work. To avoid the divergence of the coupling residual for challenging cases (e.g., low structure–fluid density ratio), additional sub-schemes have been implemented to bring robustness and numerical stability to the FSI coupling. For instance, we switch to constant under-relaxation if Aitken's method diverges. Second, the present study also aims to generate new numerical datasets while extending the FSI benchmark proposed by Turek and Hron [10], which could serve as additional benchmark data for future studies. These datasets correspond to a wide range of mass ratio (M) and bending stiffness (K_b) of the plate. The second objective is to investigate the coupled dynamics of an elastic splitter plate attached to a cylinder, subjected to laminar flow. We consider a wide range of $M = [0.14, 20]$, $K_b = [0.0008, 0.044]$ and $U_R = [2.6, 30.3]$, at $Re = 100$, as compared to the previous reports.

2 Computational model

We employ an in-house FSI solver based on a sharp-interface IB method which was developed by Mittal and co-workers [9, 39–41]. In the present work, the implicit coupling between the flow and structural dynamics solver has been implemented with dynamic under-relaxation [42] and several code validations against FSI benchmarks are carried out [43]. In the following subsections, different components of the solver are described briefly. The definitions of the major symbols used in the model are given in Table 1.

2.1 Fluid dynamics

The flow is governed by the two-dimensional, unsteady, viscous, incompressible Navier–Stokes equations for a Newtonian fluid, written in dimensionless form as follows:

$$\frac{\partial u_i}{\partial x_i} = 0, \quad (6)$$

$$\frac{\partial u_i}{\partial t} + u_j \frac{\partial u_i}{\partial x_j} = -\frac{\partial p}{\partial x_i} + \frac{1}{Re} \frac{\partial^2 u_i}{\partial x_j \partial x_j}, \quad (7)$$

where $i, j = 1, 2$, and u_i , t , p and Re are velocity components, time, pressure and Reynolds number, respectively. Re is based on mean inlet flow velocity and cylinder diameter. The computational methodology to solve the above governing equations including discretization of the equations and algorithm of the flow solver has been previously well documented, and details can be found in previous papers [39–41].

To treat fluid–structure interface in the fluid domain, a sharp-interface IB method based on a multi-dimensional ghost-cell methodology developed by Mittal et al. [39] is employed. In this method, the governing equations for the fluid domain are solved on a non-uniform Cartesian grid in the Eulerian framework and the moving structure boundary is tracked within a Lagrangian framework. A schematic of the ghost-cell method is shown in Fig. 1a. The cells whose centers are located inside the structure are identified as structure cells and the other cells outside the structure are identified as fluid cells. A structure cell which has at least one fluid cell as a neighbor is called a ghost cell. A normal probe is extended from a ghost cell to intersect with the fluid–structure interface at a point, defined as body intercept point (Fig. 1a). The probe is extended into the fluid to the image point such that the body-intercept lies midway between the image and ghost points, as shown in Fig. 1a. The kinematic boundary condition at the interface is prescribed by specifying an appropriate value at this ghost cell.

While tackling a moving fluid–structure interface, the sharp-interface IB methods are usually prone to spurious pressure oscillations due to the generation of “fresh” and “dead” cells [39]. The fresh (dead) cells are that fluid (solid) cells which were solid (fluid) cells in the previous time step. A cut-cell method proposed by Seo and Mittal [40] is utilized to reduce the spurious pressure oscillations generated by fresh and dead cells.

2.2 Structure dynamics

Here, we briefly describe governing equation and constitutive model for the structure and more details are given in

our previous paper [12]. The Navier equations, i.e., momentum balance equation in Lagrangian form, are expressed as follows:

$$\rho_s \frac{\partial^2 d_i}{\partial t^2} = \frac{\partial \sigma_{ij}}{\partial x_j} + \rho_s f_i, \tag{8}$$

where i and j range from 1 to 3, ρ_s is the structure density, d_i is the displacement component in the i direction, t is the time, σ_{ij} is the Cauchy stress tensor and f_i is the body force component in the i direction. The displacement vector $\mathbf{d}(\mathbf{x}, t)$ describes the motion of each point in the deformed structure as a function of space \mathbf{x} and time t .

We employ Saint Venant–Kirchhoff material for the structure that considers geometric nonlinearity for a linear elastic material. The constitutive relation between the stress and the strain is based on Green–Lagrangian strain tensor \mathbf{E} and second Piola–Kirchhoff stress tensor $\mathbf{S}(\mathbf{E})$ as a function of \mathbf{E} . The second Piola–Kirchhoff stress tensor can be expressed in terms of the Cauchy stress tensor σ as follows:

$$\mathbf{S} = J\mathbf{F}^{-1}\boldsymbol{\sigma}\mathbf{F}^{-T}, \tag{9}$$

where J is the determinant of the deformation gradient tensor \mathbf{F} . The Green–Lagrangian strain tensor \mathbf{E} is defined as follows:

$$\mathbf{E} = \frac{1}{2}(\mathbf{F}^T\mathbf{F} - \mathbf{I}). \tag{10}$$

The input parameters to the constitutive model are Young’s modulus (E) and Poisson ratio (ν). The Navier equations are solved using Galerkin finite-element method, implemented in Tahoe, an open-source, Lagrangian, three-dimensional, finite-element solver. (Tahoe was developed at Sandia National Labs, USA.) The details of the numerical methodology have been documented in previous papers [12, 44].

2.3 Implicit coupling with dynamic under-relaxation

In order to couple the flow and structural solvers, the continuity of velocity on the fluid–structure interface, i.e., no-slip condition, is applied for the fluid domain, expressed as follows:

$$u_{i,f} = \dot{d}_{i,s}, \tag{11}$$

where subscripts f and s denote the fluid and structure, respectively. The continuity of the traction is prescribed at the fluid–structure interface, given by,

$$\sigma_{ij,f}n_j = \sigma_{ij,s}n_j, \tag{12}$$

where n_j is local normal pointing outward on the fluid–structure interface in the fluid domain. The pressure on the interface is computed using interpolated pressure at the boundary intercept points via a trilinear interpolation (bilinear interpolation for 2D), as described by Mittal et al. [39].

The flow and structural solvers are coupled using an implicit partitioned approach using a constant value of under-relaxation, as described by Bhardwaj and Mittal [9]. In the present work, we implement dynamic under-relaxation factor (ω), estimated using Aitken’s method. In the implicit coupling, the flow solution is marched by one time step with the current deformed shape of the structure and the velocity of the fluid–structure interface acts as the boundary condition in the flow solver, as shown in the flowchart in Fig. 1b. The structural solver is marched by one time step with the updated fluid dynamic forces. The FSI convergence is declared if L_2 norm of the displacement or velocity of the interface reduces below a preset value (Fig. 1b).

In Aitken’s method, two previous FSI sub-iterations are used to predict a better value of ω . The expression of ω at a given FSI sub-iteration k is given by [17],

$$\omega_k = -\omega_{k-1} \frac{(\mathbf{R}_{k-1})^T(\mathbf{R}_k - \mathbf{R}_{k-1})}{\|\mathbf{R}_k - \mathbf{R}_{k-1}\|^2}, \tag{13}$$

where \mathbf{R} is the interface residual vector and is defined as follows:

$$\mathbf{R} = \mathbf{I}_{\text{new}} - \mathbf{I}_{\text{old}}, \tag{14}$$

where \mathbf{I} is an interface variable, namely position (\mathbf{X}), velocity (\mathbf{V}) and acceleration (\mathbf{A}) of the interface. \mathbf{R} is the difference between new and old values of \mathbf{I} in a sub-iteration. Each variable is composed of two components (3 in three-dimensional); thus, we could use 6 (9 in three-dimensional) different variables to compute ω , using Eq. 13. In the present work, we used velocity of the interface in y -direction to compute ω .

We start the FSI sub-iterations with a small initial guess of ω (say ω_0). A better guess of ω_0 is the value obtained using constant under-relaxation value, to achieve the FSI convergence. As shown in the flowchart in Fig. 1b, we calculate FSI residual (r) based on \mathbf{X} and \mathbf{V} over successive sub-iterations and convergence is declared if the residual reduces below a defined threshold value. We compute ω at a given sub-iteration k using Eq. 13 and keep revising the position and velocity of the fluid–structure interface (\mathbf{X} and \mathbf{V}) until the convergence is achieved in a given time-step.

Aitken’s method is exact for linear systems, implying that three iterations (two previous guesses plus one for Aitken) are needed for the convergence of a linear

system in a given time step. However, due to the large nonlinearity of the present FSI system, the coupling may diverge due to the large value of ω , predicted by the Aitken's method. To circumvent this problem and to ensure convergence, we implement the following two sub-schemes in the algorithm. First, the value of ω is restricted in a defined range, $[\omega_{\min}, \omega_{\max}]$. Thus, a large prediction of ω by the Aitken's method is superseded by ω_{\max} . Second, in case of a divergence even with ω_{\max} , we switch to constant under-relaxation value for few sub-iterations, say N_{safe} and use a smaller under-relaxation value, say ω_{safe} . We switch back to the dynamic under-relaxation after N_{safe} iterations. We have used $N_{\text{safe}} = 5$ and $\omega_{\text{safe}} = \omega_0 = 0.1$ in the present work. The improvement in the FSI convergence as well as numerical stability for a test case is discussed in Sect. 3.4.

3 Benchmarking and testing of the FSI solver

3.1 Grid-size independence study for fluid domain

We examine grid-size convergence for the FSI benchmark problem, proposed by Turek and Hron [10], in an *open domain* instead of a channel. As shown schematically in Fig. 2, we consider a thin, elastic splitter plate with dimensions $3.5D \times 0.2D$, mounted at the lee side of a rigid cylinder of diameter, D . The domain length and width are $(S_1 + S_2)$ and S_3 , respectively, where S_1 , S_2 and S_3 are taken as $5.5D$, $14D$ and $12D$, respectively. The center of the cylinder is $(S_1, S_3/2)$.

The boundary conditions for the present work are illustrated in Fig. 2. Inflow and outflow velocity boundary conditions are prescribed at the left and right boundary,

respectively. At left boundary, the following inlet velocity is prescribed, $u_i = (1, 0)$. At the top and bottom boundaries of the domain, zero shear stress boundary condition is prescribed. No slip is applied on the fluid–structure interface. The following values are considered for the simulation setup, $D = 1$ and $Re = 100$, based on the cylinder diameter and uniform velocity at the inlet. The dimensionless Young's modulus, structure to fluid density ratio and Poisson ratio are taken as 100, 1.4×10^3 , 10 and 0.4, respectively.

Five cases of non-uniform Cartesian grids in the fluid domain with the following points are considered for carrying out grid-size independence study: 193×65 , 257×97 , 321×161 , 385×193 and 481×193 . A high resolution of the grid is incorporated into the region where the plate movement is expected (Fig. 3a) and a non-uniform grid stretching is used from this region to the boundary. The minimum grid sizes in x - and y -directions are kept same, $\Delta x_{\min} = \Delta y_{\min}$, in each case and are listed in Table 2. The ratio of minimum grid size, $\zeta = \Delta x_{\min}^k / \Delta x_{\min}^{k+1}$, between successive meshes is also listed in Table 2, where Δx_{\min}^k is the grid size of case k . ζ is around 1.3, except for the coarsest mesh considered (for case 1, $\zeta = 1.67$). The time step for these unsteady simulations is set to $\Delta t = 0.01$, based on a time-step independence study (not shown here).

The comparison of the time-varying Y -displacements of the tip of the plate obtained for different grids is shown in Fig. 4a. We note minor differences in the maximum tip displacement for different cases plotted in the inset. Computed amplitudes of the vibration of the plate ($A_{V_{\text{tip}}}$) for different grids are also listed in Table 2. To quantify the grid size convergence, L_2 norm of the errors in the amplitude of the displacement signal ($A_{V_{\text{tip}}}$) with respect to the finest grid is estimated and is given in Table 2. The L_2 error norms

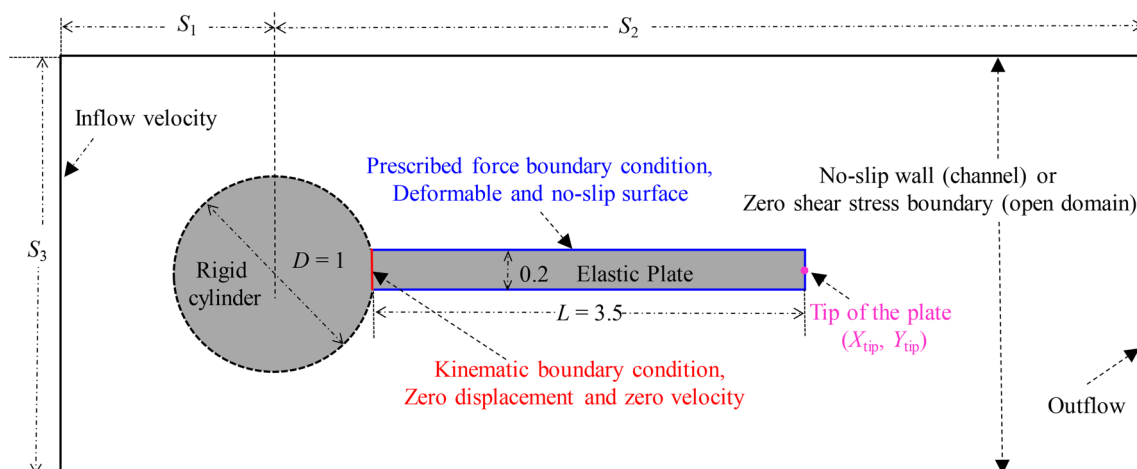


Fig. 2 Schematic of computational domain with details of the boundary conditions considered for the validation with FSI benchmark proposed by Turek and Hron [10] and for analyzing the FIV of the plate in an open domain

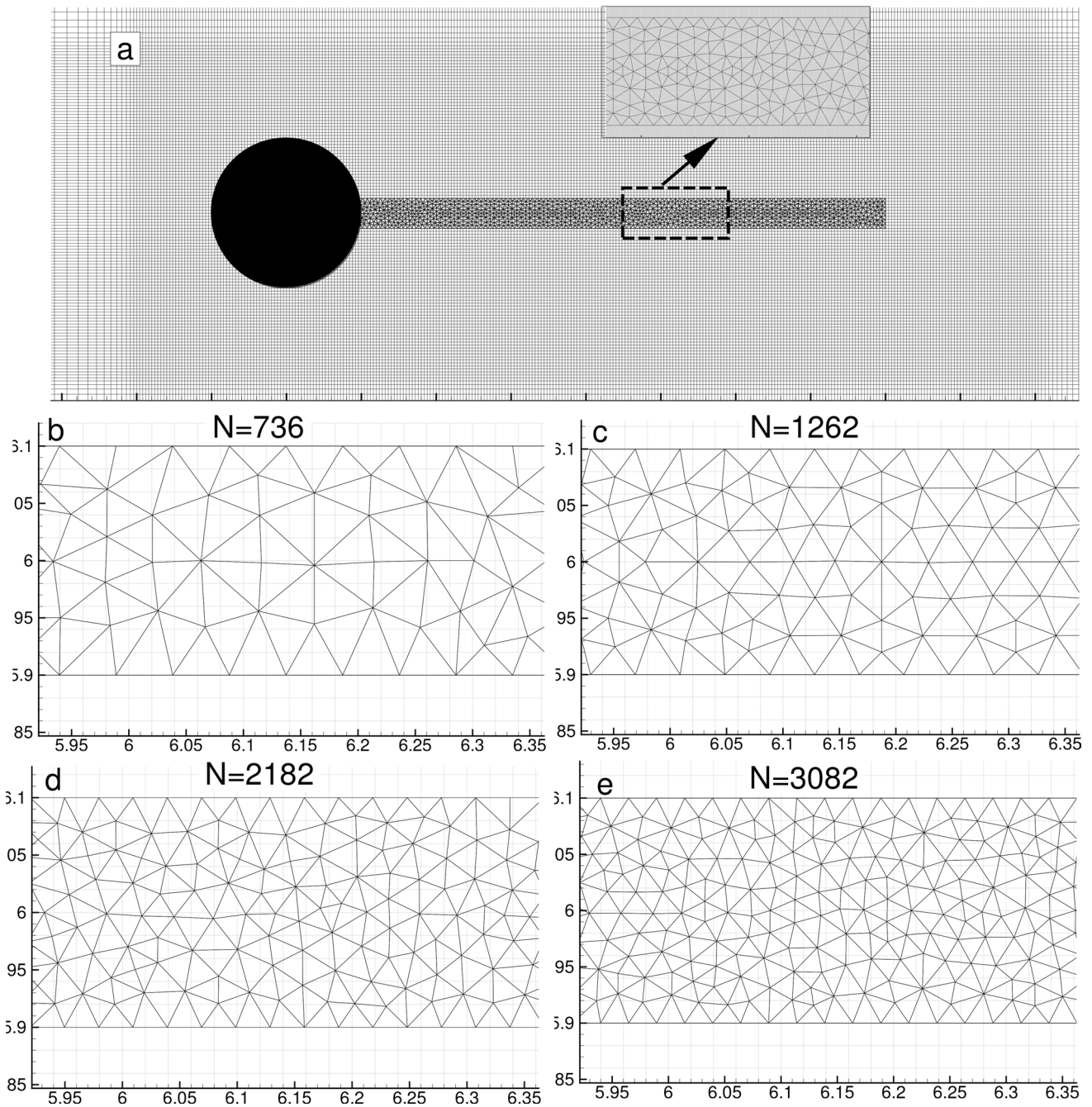


Fig. 3 **a** Finite-element grid of the plate immersed in a non-uniform Cartesian grid for the fluid domain. A uniform grid is used in the region in the fluid domain in which the plate is expected to move and non-uniform grid stretching is used from this region to the boundaries of the computational domain. Inset shows zoomed-

in view of the finite-element grid in the plate. **b–e** Zoomed-in view of the finite-element grid for different cases of the grids considered in the plate, for carrying out grid-size resolution study. The number of finite elements (N) is specified for each case

are plotted against the grid size ($\Delta x_{\min} = \Delta y_{\min}$) in Fig. 4b on a log–log scale. The errors approximately reduce along a line of slope 2, implying a second-order accuracy of the coupled FSI solver. The error in the case of 385×193 grid is one order of magnitude lesser than the coarsest grid considered (Table 2). Therefore, 385×193 non-uniform

Cartesian grid with $\Delta x_{\min} = 0.02$ and $\Delta y_{\min} = 0.02$ was selected for all the simulations presented in Sect. 4.

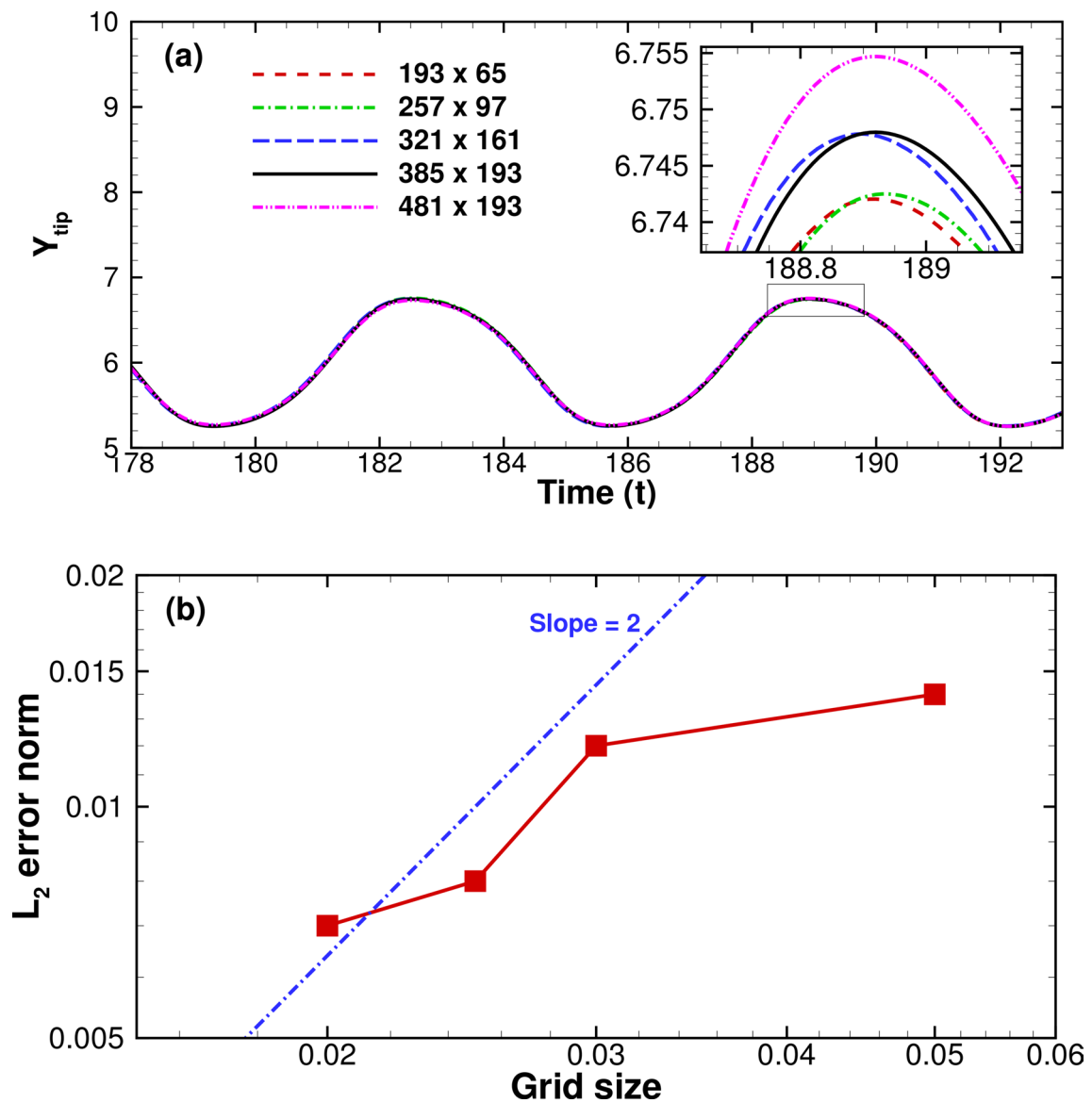


Fig. 4 Grid size convergence study for the fluid domain **a** Comparison of the time-varying cross-stream displacement of the plate tip (Y_{tip}) as a function of different grid resolutions used in the fluid domain. **b** Variation of computed L_2 error norm of A_{Ytip} of the grids

considered against the grid size ($\Delta x_{min} = \Delta y_{min}$). The errors are computed with respect to the finest grid examined, 481×193 corresponding to $\Delta x_{min} = 0.015$

3.2 Domain-size independence study

In order to test domain size independence, we vary the size, $(S_1 + S_2) \times S_3$, and consider four domains of sizes, $19.5D \times 12D$, $30D \times 12D$, $40D \times 12D$ and $50D \times 20D$. Other simulation parameters are kept the same as described in Sect. 3.1. We kept $S_1 = 5.5D$ for all cases and varied S_2 and S_3 to study the domain size independence, as given in Table 3. Simulated values of the amplitude of the Y-displacement (A_{Ytip}) obtained for all cases are listed in Table 3, and we note minor differences in the values of the A_{Ytip} . The percentage differences in A_{Ytip} with respect to the

biggest domain considered ($50D \times 20D$) for the rest of the domains are also listed in Table 3. The magnitude of the percentage difference concerning the $19.5D \times 12D$ domain is lesser than 1%. Therefore, $19.5D \times 12D$ domain is subsequently used for simulations presented in Sect. 4.

3.3 Grid-size independence study for structure domain

We perform structural grid-size convergence study in an open domain with a 385×193 grid in the fluid domain and consider four different grids composed of triangular

finite elements in the plate (Fig. 3b–e). The numbers of finite triangular elements (N) in different structural grids considered are listed in Table 4. The boundary conditions, domain size and simulation parameters are kept the same, as discussed in Sect. 3.1. The comparison of the time-varying displacements (Y_{tip}) obtained for the different structural grids is shown in Fig. 5a. The comparison shows minor differences in the maximum displacement, as shown in the inset of the figure. Computed values of $A_{Y_{\text{tip}}}$ for all cases are also given in Table 4. In order to quantify the grid convergence, L_2 norms of the error with respect to the finest grid ($N = 3082$) are listed in Table 4 and are plotted against N on a log–log scale in Fig. 5b. The errors approximately decay along a line of slope 2, implying a second-order accuracy. Since the error for $N = 2182$ is one order of magnitude smaller (Table 4) than the coarsest grid considered ($N = 736$), we choose $N = 2182$ grid for the simulations presented in Sect. 4.

3.4 Testing of faster convergence by using dynamic under-relaxation

We test the improvement in the convergence of the implicit coupling by dynamic under-relaxation scheme, described in Sect. 2.3. The test problem is chosen as FSI benchmark problem proposed by Turek and Hron [10] in an *channel*, described in the previous section. We used velocity of the interface in y -direction to compute ω (Eq. 13) for the dynamic under-relaxation, and the tolerance for the convergence is set to 2×10^{-4} . The value of ω at which the constant under-relaxation converges for this problem is around 0.1. In order to demonstrate the advantage offered by the dynamic under-relaxation, we compare the following three cases: (1) constant under-relaxation, $\omega = 0.1$; (2) dynamic under-relaxation, $\omega_{\text{min}} = 0.1$ and $\omega_{\text{max}} = 0.4$; and (3) dynamic under-relaxation with $\omega_{\text{min}} = 0.05$ and $\omega_{\text{max}} = 0.8$.

Computed y -displacement of the tip of the plate is shown in Fig. 6a. The plate attains a self-sustained periodic oscillation with a constant amplitude and frequency after $t \approx 60$. We examine the FSI convergence history at four time instances, t_1 to t_4 (shown by black dots in Fig. 6a), in a cycle of plate oscillation. The variation of the FSI residual with sub-iterations is compared for constant and dynamic under-relaxation schemes for the time instances in Fig. 6b–e. It is noted that residual decreases much faster with dynamic ω in cases (2) and (3) as compared to constant under-relaxation, case (1), for all time instances considered. The better performances of the latter two cases are almost similar at all instances in a typical cycle of the oscillation. The computed average numbers of iterations for one cycle of plate oscillation in cases (1), (2) and (3) are around 76, 39 and 28, respectively. This shows a reduction

of around three and two times in the number of sub-iterations in cases (2) and (3), respectively, as compared to the case (1). On comparing cases (2) and (3), we note that the range of ω considered also influences the number of sub-iterations in the dynamic under-relaxation method. A linear variation of the residual (say between 15 and 20 sub-iterations at t_1) shows that the method uses a constant value of the under-relaxation, implying that the coupling scheme avoids the possible divergence. Overall, we demonstrate a reduction in FSI sub-iterations by three times using the dynamic under-relaxation scheme. The revised method ensures better numerical stability of the FSI solver at low structure–fluid density ratio and accelerates the convergence of the implicit coupling.

3.5 Code validations

The present FSI solver has been extensively validated in previous studies. The flow solver was validated by Mittal et al. [39] for benchmark CFD problems such as the flow past a circular cylinder, sphere, airfoil, suddenly accelerated normal plate and suddenly accelerated circular cylinder. Further, Kundu et al. [34] validated the flow solver for pulsatile inflow past a cylinder in a channel. Large-scale FID of a thin, elastic splitter plate was validated against the FSI benchmark problem proposed by Turek and Hron [10], Bhardwaj and Mittal [9] and Kundu et al. [34]. Recently, the code was validated for vortex-induced vibration of a circular cylinder [45] and the FID of a viscoelastic splitter plate [46]. In the following subsections, first, we present validations of the large-scale FID module of the in-house solver, presented in Sect. 2, for the FSI benchmarks proposed by Turek and Hron [10] and Wall and Ramm [47]. We used grid size established in Sects. 3.1 and 3.3 for the fluid and structure domain, respectively.

3.5.1 Splitter plate attached to the circular cylinder

We carried out the validation proposed by Turek and Hron [10], in which an elastic plate is mounted on the lee side of a rigid cylinder in a channel (Fig. 2). The length and width of the channel are considered as $S_1 + S_2 = 20D$ and $S_3 = 4.1D$, respectively, shown in Fig. 2. The center of the cylinder is $(2D, 2D)$. The parabolic inflow boundary condition was imposed. The material parameters are taken as follows: Poisson ratio = 0.4, dimensionless Young's modulus (E) = 1400 and the structure to fluid density ratio of $\rho = 10$. Based on the grid-size independence test presented in Sect. 3.1, a non-uniform Cartesian mesh with 385×161 nodes was used for simulation with $\Delta x_{\text{min}} = \Delta y_{\text{min}} = 0.02$ and non-dimensional time step of $\Delta t = 0.01$.

The computed displacement of the tip of the plate is periodic, and its amplitude reaches a plateau value at around $t \approx 60$ (Fig. 6a). We compare the time-varying cross-stream position of the plate tip (Y_{tip}) with the benchmark data of Turek and Hron [10] in Fig. 7. The amplitude ($A_{Y_{\text{tip}}}$) and oscillation frequency (f_p) of the plate are in excellent agreement with the published data. We also extend the benchmark in an open domain, keeping all simulation parameters the same. Zero shear stress boundary condition is applied at the top and bottom boundary (Fig. 2) in this case. The plate displacement (Y_{tip}) and its oscillation frequency (f_p) for the open domain are $0.75D$ and $0.155D/U$, which are slightly lower than the corresponding benchmark values for the channel.

3.5.2 Splitter plate attached to the square cylinder

We further validate the large-scale FID module against the benchmark problem proposed by Wall and Ramm [47]. In this problem, a thin elastic splitter plate is attached to a rigid square cylinder, as shown in Fig. 8a. The reference length is taken as the side length of the square cylinder, and the reference velocity is taken as the inlet velocity. Re based on these reference values is 333. The material parameters are taken as follows: Poisson ratio = 0.35, dimensionless Young's modulus $E = 8.1 \times 10^5$ and the structure to fluid density ratio $\rho = 84.7$. The inlet flow conditions and boundary conditions are illustrated in Fig. 8a. A non-uniform Cartesian mesh specified in the validation study has been used for this simulation, and the non-dimensional time step was set to $\Delta t = 7.5 \times 10^{-3}$. The plate reaches a self-sustained periodic state, similar to the case of an elastic plate attached to a circular cylinder. The time history of the tip displacement (Y_{tip}) is plotted in Fig. 8b. The computed plate vibration frequency, as well as the tip displacement along with published results, is listed in Table 5. We found excellent agreement between the present and published results [47–49], which further validates the present FSI solver. At the maximum tip displacement, contours of vorticity are shown at different time instances in Fig. 8c. These time instances are shown by dots in Fig. 8b. As noted from the vorticity field, vortices shed alternatively at the top and bottom of the deforming plate.

4 Analysis of FIV of an elastic splitter plate

Numerical simulations were performed for the elastic splitter plate in an open domain using the same parameters, domain size and boundary conditions, as discussed in Sect. 3.1. The effects of mass ratio (M) and bending stiffness (K_b) on the dynamics of the elastic plate as a function

of reduced velocity (U_R) are discussed in the following subsections. The definitions of these dimensionless variables are given in Table 1.

4.1 Effect of mass ratio (M)

We discuss the effect of M on the elastic splitter plate displacement ($A_{Y_{\text{tip}}}$), oscillation frequency (f_p) and wake structures, keeping K_b constant. Simulations are presented for $M = [0.143, 20.029]$ and $K_b = 0.0218$, with simulation parameters given in Table 6. Figure 9 plots amplitude of the tip of the plate, $A_{Y_{\text{tip}}}$, as a function of U_R for different cases of M . The range of U_R considered is $[2.562, 30.311]$ and U_R increases with an increase in M , as noted in Table 6. We also plot frequency ratio, f_p/f_{n1} as a function of U_R , where f_p and f_{n2} are the frequencies of the plate and its natural frequency of oscillation in second mode, assuming it as a Euler–Bernoulli beam. These frequencies are obtained by the numerical simulation and Eq. 5, respectively.

Figure 9 shows that $A_{Y_{\text{tip}}}$ increases with U_R for $0.286 \leq M \leq 2.747$, reaching a maximum value of 1.93 at $M = 2.747$ and then decreases with U_R in the range $2.747 \leq M \leq 14.306$. The frequency ratio increases with M (or U_R) for $0.286 \leq M \leq 1.717$ and is around 0.8–0.9, i.e., closer to unity for $1.717 < M < 3.434$. Figure 9 shows that a larger amplitude oscillation occurs for the cases where $f_p/f_{n2} \approx 0.8$ –0.9. This is called as lock-in condition (discussed in detail in the next section), and we plot a dotted line to denote the lock-in condition where $f_p/f_{n2} = 1$. The curve starts to deviate from the dotted line over the mass ratio range $3.434 \leq M \leq 5.723$. At $M \geq 17.167$, $A_{Y_{\text{tip}}}$ reduces to zero.

4.1.1 Lock-in condition

In the case of vortex-induced vibration (VIV) of an elastically mounted cylinder, the lock-in occurs if the vortex shedding frequency changes (and locks) to match the natural frequency of spring in vacuum [50] and the cylinder oscillates with a larger amplitude. In the present case, the simulated flow over a rigid splitter plate of length $L/D = 3.5$ does not show any vortex shedding at $Re = 100$. In the case of a rigid and sufficiently long splitter plate mounted on the lee side of the cylinder, the plate inhibits flow instabilities in the wake, and vortex shedding is suppressed. However, in the case of a shorter rigid plate, the shedding may occur. Therefore, we extend the definition of the lock-in in a classical VIV of a cylinder to the present FSI system, i.e., a rigid cylinder with an elastic splitter plate. In the latter, vortex shedding frequency of the FSI system and plate oscillation frequency (f_p) are identical and lock-in is defined if the vortex shedding or plate oscillation frequency (f_p) is close to the natural frequency of the plate in

Table 1 Definitions of major symbols used in the present paper

Symbols	Definitions
A_{Ytip}	Amplitude of Y-displacement of the tip of the plate [A_{Ytip}^*/D^*]
b	Plate width [b^*/D^*]
D^*	Diameter of the cylinder [m]
E	Young's modulus [$E^*/\rho_f^*U_\infty^{*2}$]
f_{ni}	Natural frequency of the plate in vacuum [$f_{ni}^*D^*/U_\infty^*$] (Eq. 5)
f_p	Oscillation frequency of the plate [$f_p^*D^*/U_\infty^*$]
h	Plate thickness [h^*/D^*]
I^*	Moment of inertia of the plate cross section [$b^*h^{*3}/12$] [m^4]
K_b	Bending stiffness (Eq. 1)
L^*	Plate length [m]
M	Mass ratio (Eq. 2)
N	Number of triangular finite elements in plate
Re	Reynolds number [$\rho_f^*U_\infty^*D^*/\mu^*$]
Δt	Time step in the simulation
u_i	Velocity vector
U_R	Reduced velocity (Eq. 3)
U_∞^*	Inlet velocity [$m\ s^{-1}$]
\mathbf{V}	Velocity vector of fluid–structure interface
x_i	Spatial coordinates
Δx_{min}	Minimum grid size in x-direction near the plate
\mathbf{X}	Position vector of fluid–structure interface
X_{tip}	x-displacement of the tip of the plate [X_{tip}^*/D^*]
Δy_{min}	Minimum grid size in y-direction near the plate
Y_{tip}	y-displacement of the tip of the plate [Y_{tip}^*/D^*]
Greek symbols	
μ^*	Dynamic viscosity [Pa.s]
ρ	Density ratio [$\rho = \rho_p/\rho_f$]
Subscripts	
f	Fluid
p	Plate
ni	Natural frequency of mode i
Superscript	
*	Dimensional quantity
Acronyms	
ALE	Arbitrary Lagrangian–Eulerian
FID	Flow-induced deformation
FIV	Flow-induced vibration
FSI	Fluid–structure interaction
IB	Immersed boundary

vacuum for any mode (f_{ni}), where subscript i denotes the i th natural mode of the oscillation. Consequently, the plate oscillates with a larger amplitude in this condition.

We note similar characteristics for the FIV of the plate as described in the literature for the VIV of the cylinder. As discussed earlier, we note that large-amplitude oscillations

for $1.71 \leq M \leq 3.43$ if $f_p/f_{n2} \approx 0.8-0.9$, indicating a lock-in region. The deviation of the frequency ratio from unity is attributed to added mass effect at low mass ratios [51, 52]. In addition, a large reduction in A_{Ytip} from $M = 2.74$ to $M = 2.857$ in Fig. 9 is a typical transition from “upper branch” to “lower branch,” as reported for the VIV of an

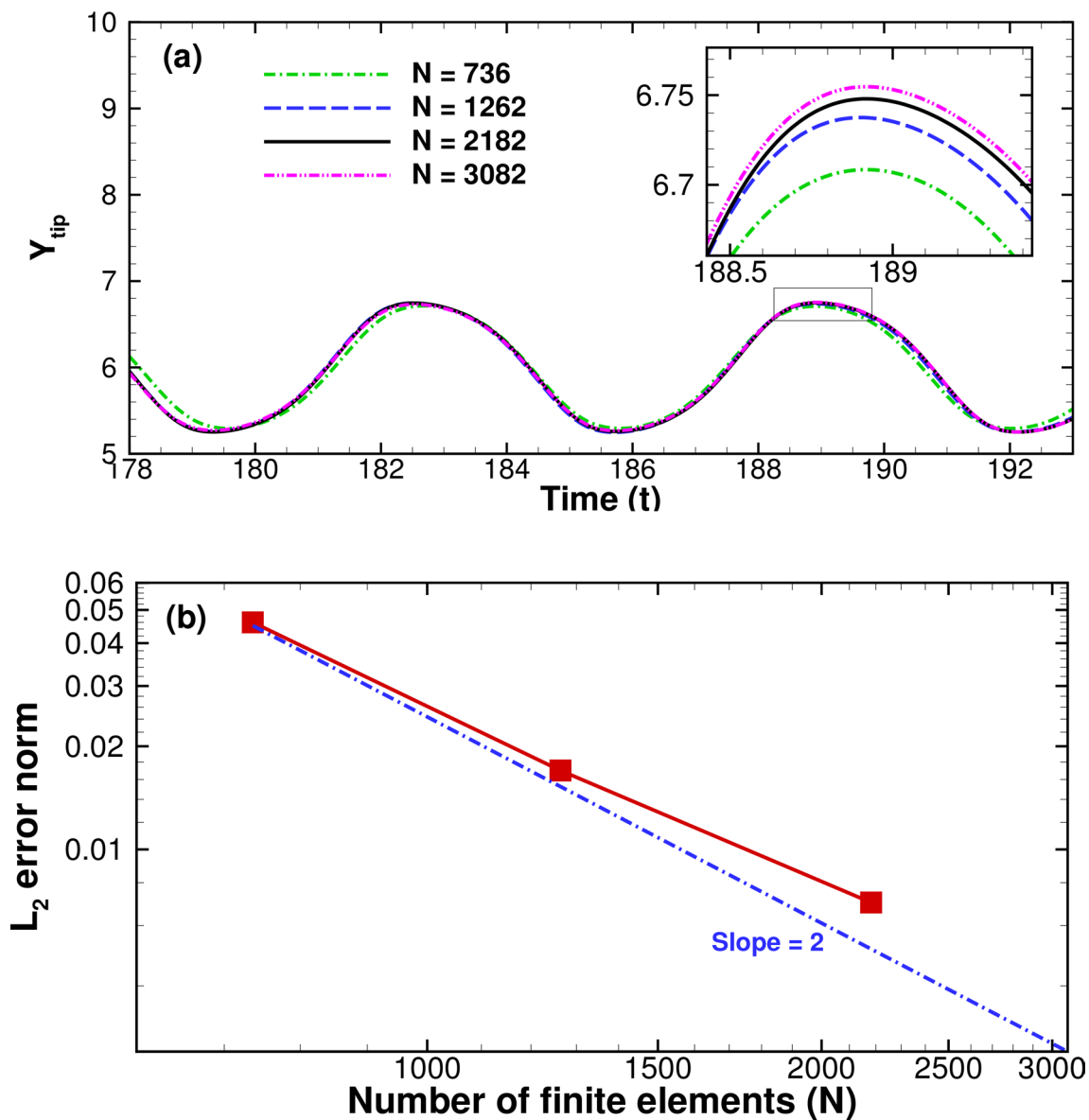


Fig. 5 Grid size convergence study for the structure domain. **a** Comparison of the time-varying cross-stream displacement of the plate tip (Y_{tip}) for different grids considered in the structure domain. The Cartesian grid for the fluid domain is kept same for each case. **b**

Variation of computed L_2 error norm of $A_{v_{tip}}$ of the grids considered against the number of finite elements (N) for the different grids. The errors are computed with respect to the finest grid examined, $N = 3082$

elastically mounted cylinder, constrained to move transverse to the flow [50].

4.1.2 Comparison of vibration characteristics of the plate and vorticity field

Figure 10 (first row) shows the comparison of the time-varying Y_{tip} for mass ratios 0.572, 2.747 and 5.723. These cases are case 4, case 13 and case 20 of Table 6. These signals are plotted after the plate reaches a self-sustained oscillation state. The computed values of the maximum

plate amplitude values are 0.75, 1.93 and 0.48, respectively. Figure 10 (second row) shows the FFT of Y_{tip} for the three cases. The dominant f_p for mass ratios 0.572, 2.747 and 5.723 is 0.159, 0.073 and 0.061, respectively. Figure 10 (second row) shows that the plate with largest deformation for $M = 2.747$ vibrates with more than one frequency. One frequency component is closer to a dominant second mode, and the other is a third harmonic of the dominant frequency. The phase plots in the third row of Fig. 10 show the axial and lateral movement of the plate tip, which are larger for $M = 2.747$ than other mass ratios because of the

Table 2 Details of hierarchy of grids considered for carrying out grid independence study for the fluid domain

Case	Grid points	Grid size	ζ	A_{Ytip}	L_2 error norm
1	193 × 65	0.050	1.67	0.741	0.014
2	257 × 97	0.030	1.20	0.743	0.012
3	321 × 161	0.025	1.25	0.747	0.008
4	385 × 193	0.020	1.33	0.748	0.007
5	481 × 193	0.015	–	0.755	–

The grid sizes in x - and y -direction is kept same where the plate is expected to move ($\Delta x_{min} = \Delta y_{min}$) and are given for all the cases. The ratios of grid sizes (ζ) of two successive cases ($\zeta = \Delta x_{min}^k / \Delta x_{min}^{k+1}$) are also listed (Δx_{min}^k is the grid size of case k). Computed amplitudes of the vibration of the plate (A_{Ytip}) for different grid sizes are given and L_2 error norms are calculated for each case relative to the finest grid

lock-in. As a result, the phase plots are wider at $M = 2.747$ and each case exhibits a limit-cycle flapping [21].

Figure 11 depicts the instantaneous vorticity field around the plate. The vorticity is plotted in Fig. 11 at three different instances, corresponding to maximum, minimum and central positions of the plate. For $M = 0.572$, the elastic splitter plate is in its self-sustained oscillation state and vortices are shed alternately (see the first column of Fig. 11). The vortex shedding shows “2S” vortex pattern, i.e., one vortex sheds from each side of the plate in a cycle [53] in the downstream. For $M = 2.747$, the elastic plate bends to a greater degree compared to the $M = 0.572$. As a result, longer vortex shedding from the elastic plate is observed, and it tends to split into two small vortices, which are not completely separated immediately. This vortex shedding flow pattern is typically similar to the 2P mode, i.e., two vortices shed from each side of the plate each time [53]. For $M = 5.723$, two positive and two negative vortices are shedding alternatively, as shown in the third column of Fig. 11. Therefore, the vortex-shedding pattern depends on the FIV of the plate.

4.2 Effect of bending stiffness (K_b)

The effect of K_b on the FIV of the elastic splitter plate is examined in this section. We consider $K_b = [0.0008, 0.0436]$ keeping the mass ratio $M = 0.572$ constant. The parameters of these simulation cases are given in Table 7. As done previously in Sect. 4.1, we plot A_{Ytip} and f_p/f_{n2} as function of U_R for different cases of K_b in Fig. 12. Note that U_R decreases with an increase in K_b , as noted in Table 7. Figure 12 shows that A_{Ytip} is negligible at large K_b (small U_R) and it increases with U_R or decreases with K_b . The frequency ratio, f_p/f_{n2} , is plotted as a function of U_R (or K_b), and a red dotted line corresponds to ratio 1, i.e., lock-in condition. A larger amplitude occurs if f_p/f_{n2} is in range of

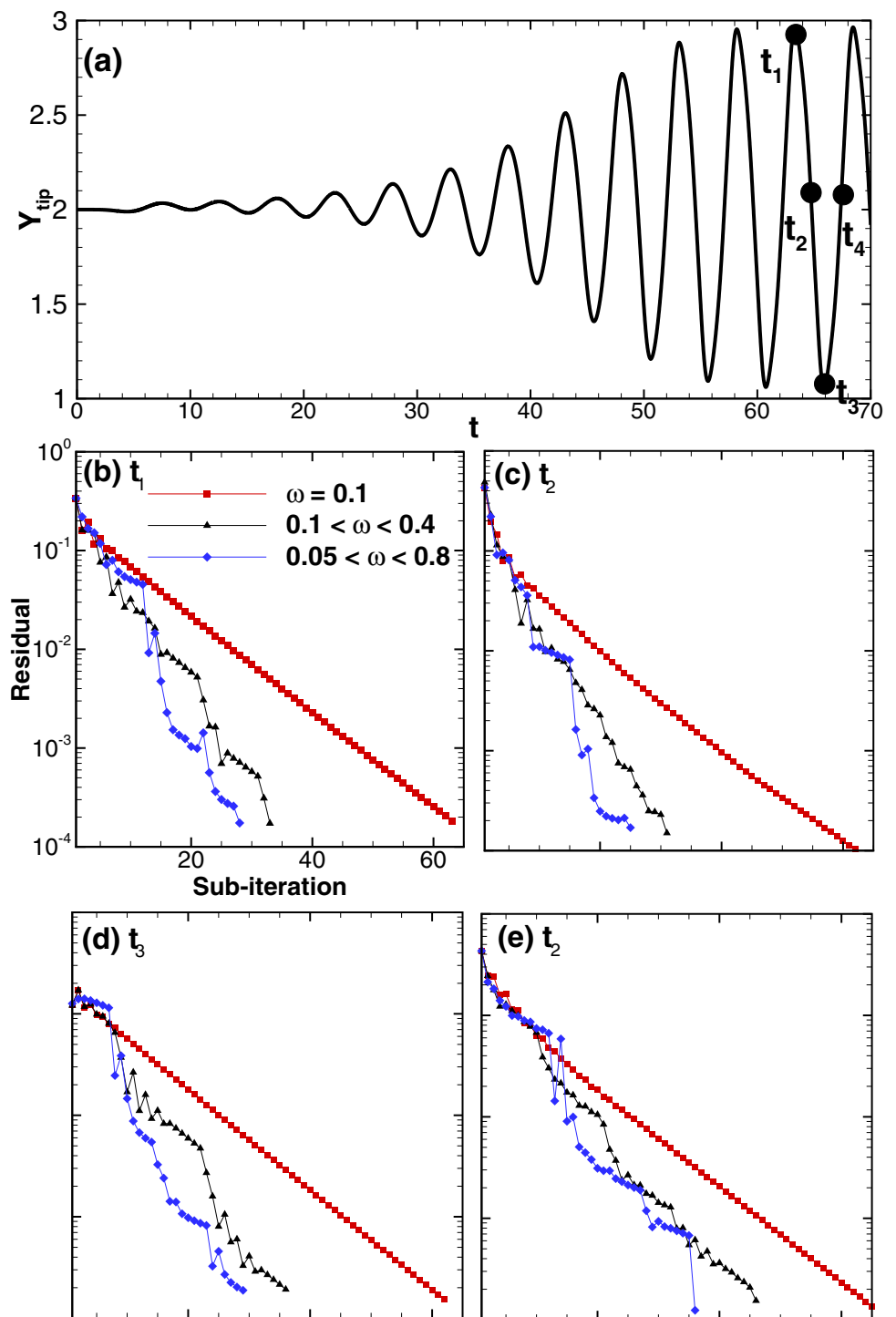
[0.9, 1.6]. The deviation of the frequency ratio from unity ($f_p/f_{n2} \approx 1.6$) is attributed to added mass effect at low mass ratios [50–52]. The plate amplitude is almost negligible for very large or very small K_b . The plate exhibits higher modes of the vibration along with the second natural mode at larger U_R (at $U_R = 15.652$ and 19.170 and desynchronizes with the wake at $U_R = 27.111$). In general, the plate exhibits similar characteristics, as seen for VIV of an elastically mounted cylinder, constrained to move transverse to the flow [50].

Figure 13 shows Y_{tip} , power spectra, phase plots of the plate in the first, second and third row, respectively. These three rows correspond to $K_b = 0.0023$ (case 29 in Table 7), 0.0109 (case 35) and 0.0218 (case 4). The dominant frequencies, plotted in Fig. 13 (second row), are closer to second-mode natural frequency in the respective cases (e.g., $f_{n2} = 0.0635$ for $K_b = 0.0023$, Eq. 5). The higher modes of the vibration are also observed for $K_b = 0.0023$ ($U_R = 15.652$). Figure 13 (third row) shows that the phase plot is wider at $K_b = 0.0023$, i.e., the plate shows larger bending as compared to other two cases. This is attributed to the lock-in condition for this case. Figure 14 shows the vorticity field for three cases of bending stiffness. Alternate vortices shed in the downstream in each case in 2S mode for all the cases [53]. The vortex structures become elongated at lower bending stiffness as compared to high bending stiffness due to the larger plate displacement.

5 Applications of present study in energy-harvesting

The present numerical data are envisioned to design MEMS-based piezoelectric energy harvesters that harness available ambient wind energy. Such miniaturized harvesters are potential candidates to replace traditional chemical batteries. In particular, they could be useful in sensors mounted on a tall bridge on which ambient fluid energy is easily available and replacement of the batteries in the sensors is expensive [54]. In general, Re is on the order of $O(100)$ – $O(1000)$ in such miniaturized devices. Table 8 summarizes recent few studies which examined the design and performance of such devices. In the present study, Re based on the plate length is 350, which is on the order of Re used in the previous studies [55–57]. Figure 15 plots amplitude of the plate tip on M - K_b plane for all cases considered in the present work and the radius of the circle represents the magnitude of the amplitude. Therefore, $(M, K_b) = (2.69, 0.0218)$ is an optimum point in Fig. 15, at which the FID of the plate is the maximum, implying that a large flow energy could be harnessed at this design point.

Fig. 6 Test of faster FSI convergence by dynamic under-relaxation. **a** Time-varying Y -displacement of tip of the plate for a typical oscillation cycle. **b–e** FSI residual variation with number of sub-iterations in the implicit coupling scheme at different time instances for density ratio, $\rho = \rho_p / \rho_f = 10$. The time instances t_1, t_2, t_3 and t_4 are shown in **a**



6 Conclusions

We have presented the development of fluid–structure interaction (FSI) solver to simulate large-scale flow-induced dynamics of a thin elastic structure. The FSI computational approach combines a sharp-interface immersed boundary (IB) method-based flow solver and an open-source finite-element-based structure solver. The implicit coupling

between the flow and structural dynamics solver has been improved with a dynamic under-relaxation scheme. The revised coupling is around two to three times faster and numerically stable, as compared to the one that uses a constant under-relaxation parameter. To bring additional numerical stability to the coupling, we have implemented an additional sub-scheme in which the solver starts using constant under-relaxation for few sub-iterations if the

Table 3 Variation in the vibration amplitude (A_{Ytip}) for different domain sizes

Cases	Domain size	S_1	S_2	S_3	A_{Ytip}	Percentage difference in A_{Ytip}
1	$19.5D \times 12D$	$5.5D$	$14D$	$6D$	0.748	-0.95%
2	$30D \times 12D$	$5.5D$	$25.5D$	$6D$	0.748	-0.95%
3	$40D \times 12D$	$5.5D$	$34.5D$	$6D$	0.747	-0.81%
4	$50D \times 20D$	$5.5D$	$45.5D$	$10D$	0.741	-

Percentage differences in the amplitude relative to the largest domain size are computed for different domains considered

Table 4 Grid-size convergence study for structure domain. The numbers of triangular finite elements (N) are given for the different grids tested

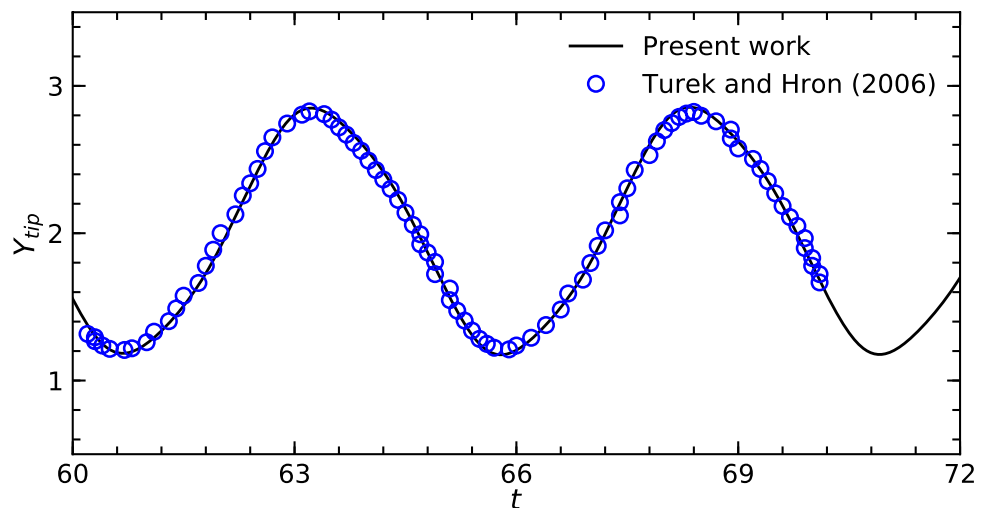
Cases	Number of finite elements (N)	A_{Ytip}	L_2 error norm
1	736	0.709	0.046
2	1262	0.738	0.017
3	2182	0.748	0.007
4	3082	0.755	-

Computed L_2 errors norm in the plate amplitude (A_{Ytip}) for different grids with respect to the finest grid examined are also listed

dynamic under-relaxation scheme diverges. The solver was validated against two-dimensional FSI benchmark problems in which a thin elastic plate is attached to a circular and square cylinder, and attains self-sustained oscillation. The present study reports new numerical data-sets while extending the FSI benchmark proposed by Turek and Hron [10], which could serve as additional benchmark data for future studies. In particular, we report a case with a larger mass ratio for FIV of a splitter plate in which tip displacement is twice larger than in the FSI benchmark proposed by Turek and Hron [10].

We have employed the FSI solver to simulate and analyze the dynamics of an elastic splitter plate attached to a rigid circular cylinder that is subjected to two-dimensional laminar flow. The effect of mass ratio (M) and bending stiffness (K_b) on the FSI response is studied at $Re = 100$. Here, Re is based on free-stream velocity and cylinder diameter. We vary M , K_b and U_R in the ranges [0.14, 20], [0.0008, 0.044] and [2.6, 30.3], respectively, noting that these ranges cover a high-amplitude FSI response. The plate amplitude and oscillation frequency are found to be a function of M and K_b . The time-varying displacement of the tip of the plate, power spectra of the displacement signal, phase plots of the plate tip displacement and the wake structure are examined to quantify the results. The largest amplitude of the plate is found to be for the lock-in region at which the natural frequency of the plate in a given fluid synchronizes with the oscillation frequency of the plate. This behavior is consistent with the classical vortex-induced vibration of a rigid cylinder. In closure, the present results provide fundamental insights into the flapping of an elastic splitter plate attached to a rigid circular cylinder, which could prove useful to the design of elastic plates for energy harvesting and thermal augmentation applications.

Fig. 7 Comparison of the computed tip displacement in Y-direction of the thin elastic splitter attached to the cylinder against the benchmark results of Turek and Hron [10]



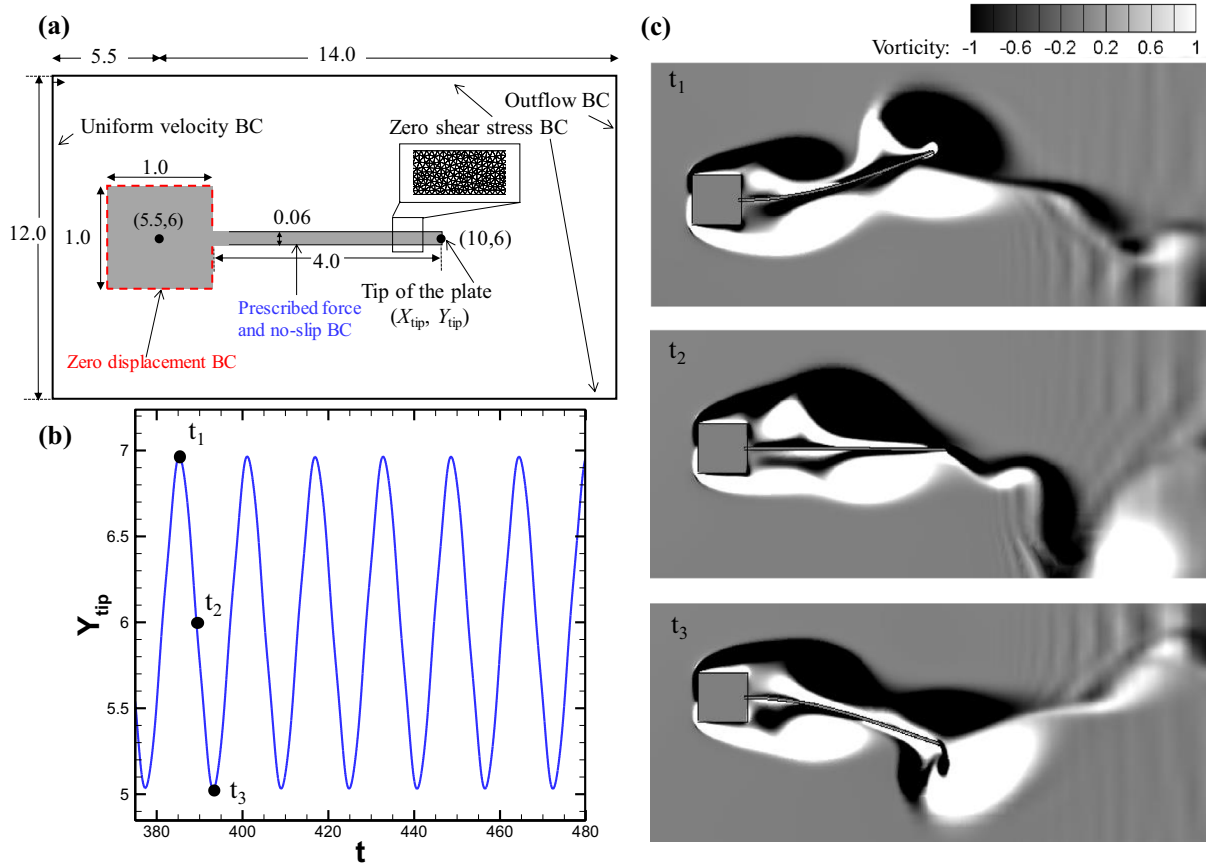


Fig. 8 **a** Schematic of FSI benchmark problem proposed by Wall and Ramm [47]. A thin elastic splitter plate is attached on the lee side of a square cylinder, subjected to laminar flow. **b** Time-varying

tip displacement in Y -direction after the plate reaches self-sustained oscillation. **c** Vorticity field at three different time instances t_1, t_2 and t_3 , as shown by black dots in **b**

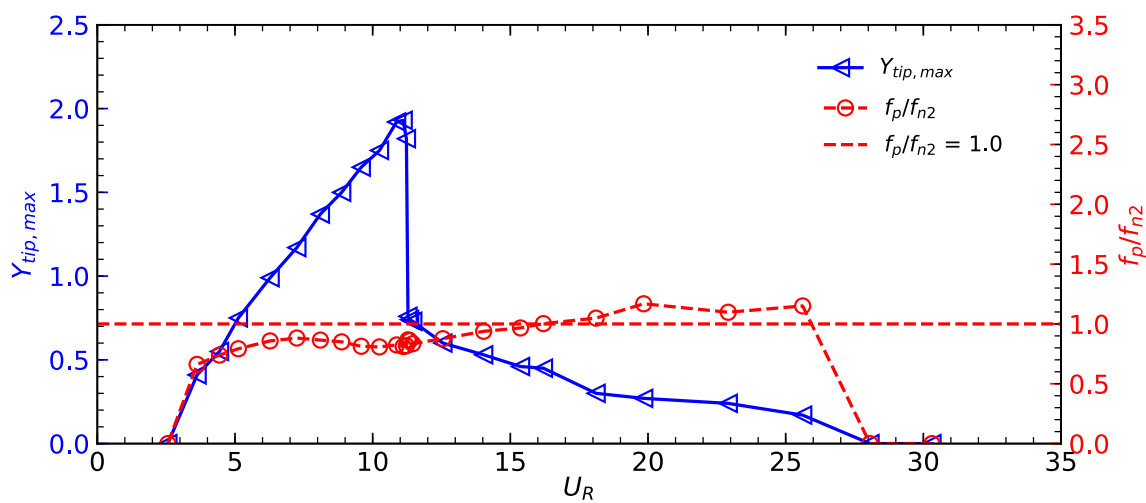


Fig. 9 Computed values of the plate amplitude ($Y_{tip,max}$) as a function of reduced velocity (U_R). The mass ratio was varied and bending stiffness is kept fixed at $K_b = 0.0218$ for the cases plotted here.

Ratio of plate oscillation frequency and second-mode natural frequency of the plate in vacuum (f_p/f_{n2}) is plotted for all cases. A dotted line at $f_p/f_{n2} = 1$ is also shown

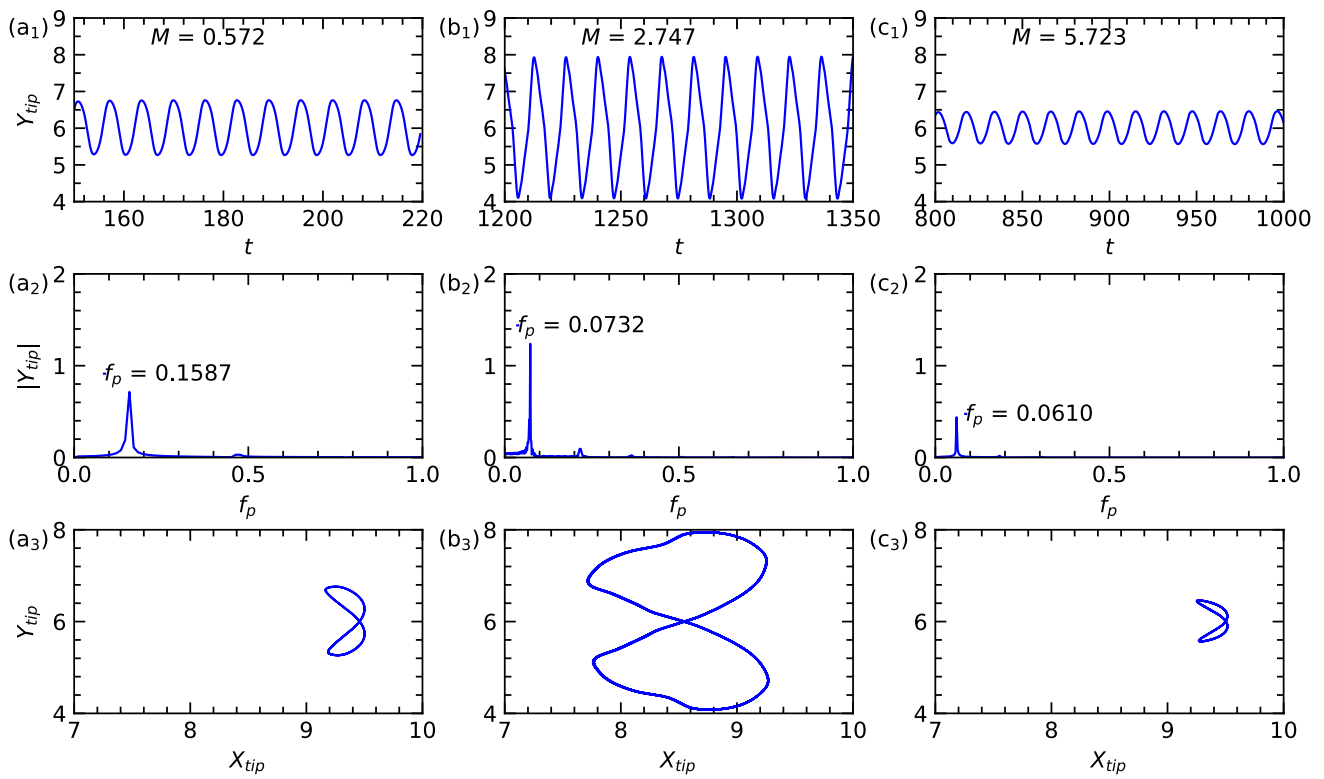


Fig. 10 Comparison of tip displacement Y_{tip} (first row), power spectra (second row) and phase-plane plots (third row) for three cases of mass ratios, $M = 0.572, 2.747$ and 5.723 . The bending stiffness

is kept same, $K_b = 0.0218$. Phase-plane plots are shown after the plate amplitude reaches a plateau value

Table 5 Comparison of computed dimensionless amplitude ($A_{Y_{tip}}$) and frequency (f_p) of a thin splitter plate attached on a square cylinder at $Re = 100$ with published data

Study	f_p	$A_{Y_{tip}}$
Present work	0.0637	0.97
Olivier et al. [48]	0.0617	0.95
Habchi et al. [49]	0.0634	1.02
Wall and Ramm [47]	0.0581	1.22

The FSI benchmark was proposed by Wall and Ramm [47]

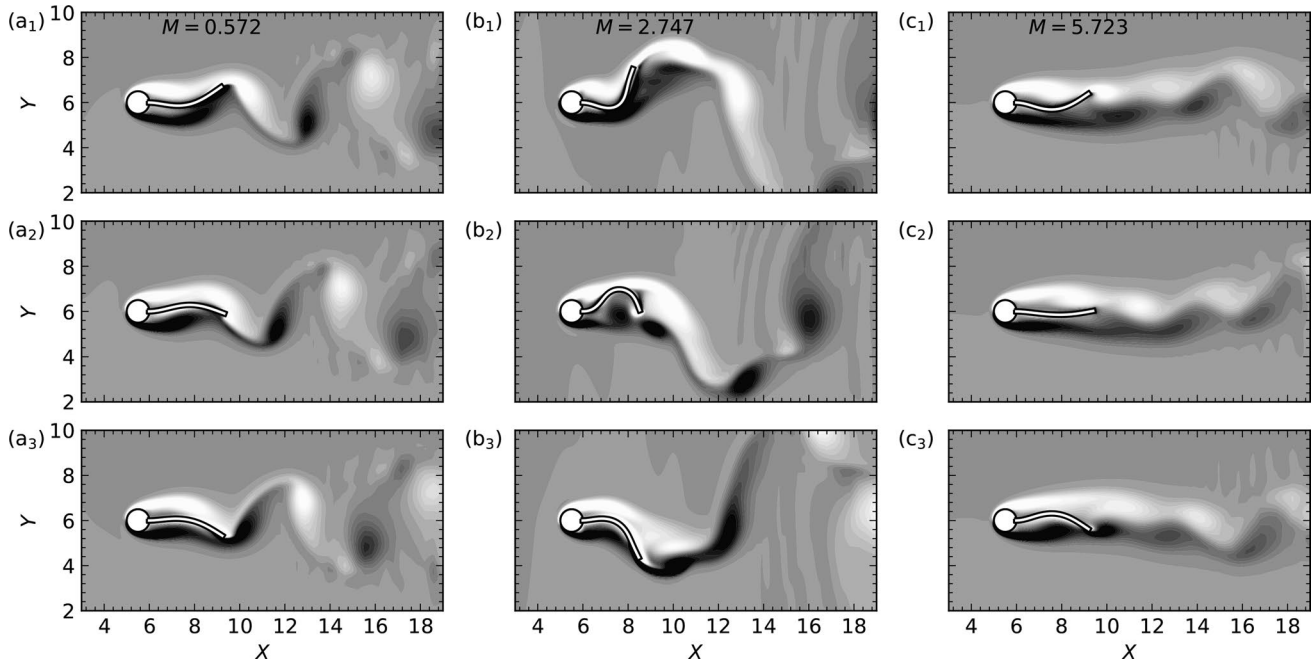


Fig. 11 Comparison of vorticity field at different time instances for three different mass ratios $M = 0.572, 2.747$ and 5.723 . The bending stiffness is kept same, $K_b = 0.0218$. The color map range is $[-2, 2]$

Table 6 Input parameters for the set of simulations to studying the effect of mass ratio, M , for fixed bending stiffness, K_b

Case number	E	h	ρ	M	K_b	U_R	A_{Ytip}	f_p
1	1400	0.2	2.5	0.143	0.0218	2.562	0	0
2	1400	0.2	5.0	0.286	0.0218	3.623	0.41	0.183
3	1400	0.2	7.5	0.429	0.0218	4.437	0.55	0.167
4	1400	0.2	10.0	0.572	0.0218	5.123	0.75	0.158
5	1400	0.2	15.0	0.859	0.0218	6.275	0.99	0.137
6	1400	0.2	20.0	1.145	0.0218	7.246	1.17	0.122
7	1400	0.2	25.0	1.431	0.0218	8.101	1.37	0.107
8	1400	0.2	30.0	1.717	0.0218	8.874	1.5	0.096
9	1400	0.2	35.0	2.003	0.0218	9.585	1.65	0.085
10	1400	0.2	40.0	2.289	0.0218	10.247	1.75	0.079
11	1400	0.2	45.0	2.576	0.0218	10.869	1.92	0.076
12	1400	0.2	47.0	2.690	0.0218	11.107	1.93	0.0732
13	1400	0.2	48.0	2.747	0.0218	11.225	1.82	0.073
14	1400	0.2	48.5	2.775	0.0218	11.283	0.76	0.077
15	1400	0.2	49.0	2.804	0.0218	11.341	0.74	0.076
16	1400	0.2	50.0	2.861	0.0218	11.456	0.73	0.073
17	1400	0.2	60.0	3.434	0.0218	12.550	0.60	0.070
18	1400	0.2	75.0	4.292	0.0218	14.031	0.53	0.067
19	1400	0.2	90.0	5.150	0.0218	15.370	0.46	0.063
20	1400	0.2	100.0	5.723	0.0218	16.202	0.45	0.061
21	1400	0.2	125.0	7.153	0.0218	18.114	0.30	0.058
22	1400	0.2	150.0	8.584	0.0218	19.843	0.27	0.059
23	1400	0.2	200.0	11.445	0.0218	22.913	0.24	0.048
24	1400	0.2	250.0	14.306	0.0218	25.617	0.17	0.045
25	1400	0.2	300.0	17.167	0.0218	28.062	0	0
26	1400	0.2	350.0	20.029	0.0218	30.311	0	0

Table 7 Input parameters for the set of simulations to studying the effect of bending stiffness, K_b , for fixed mass ratio, M

Case number	E	h	ρ	M	K_b	U_R	A_{Ytip}	f_p
27	50	0.2	10.0	0.572	0.0008	27.111	0.010	0.116
28	100	0.2	10.0	0.572	0.0016	19.170	1.150	0.087
29	150	0.2	10.0	0.572	0.0023	15.652	1.242	0.098
30	250	0.2	10.0	0.572	0.0039	12.124	1.244	0.095
31	300	0.2	10.0	0.572	0.0047	11.068	1.214	0.102
32	350	0.2	10.0	0.572	0.0055	10.247	1.185	0.104
33	400	0.2	10.0	0.572	0.0062	9.585	1.159	0.110
34	560	0.2	10.0	0.572	0.0087	8.101	1.070	0.121
35	700	0.2	10.0	0.572	0.0109	7.246	1.000	0.122
36	933	0.2	10.0	0.572	0.0145	6.276	0.905	0.137
4	1400	0.2	10.0	0.572	0.0218	5.123	0.753	0.158
37	1866	0.2	10.0	0.572	0.0291	4.438	0.560	0.173
38	2800	0.2	10.0	0.572	0.0436	3.623	0.000	0.000

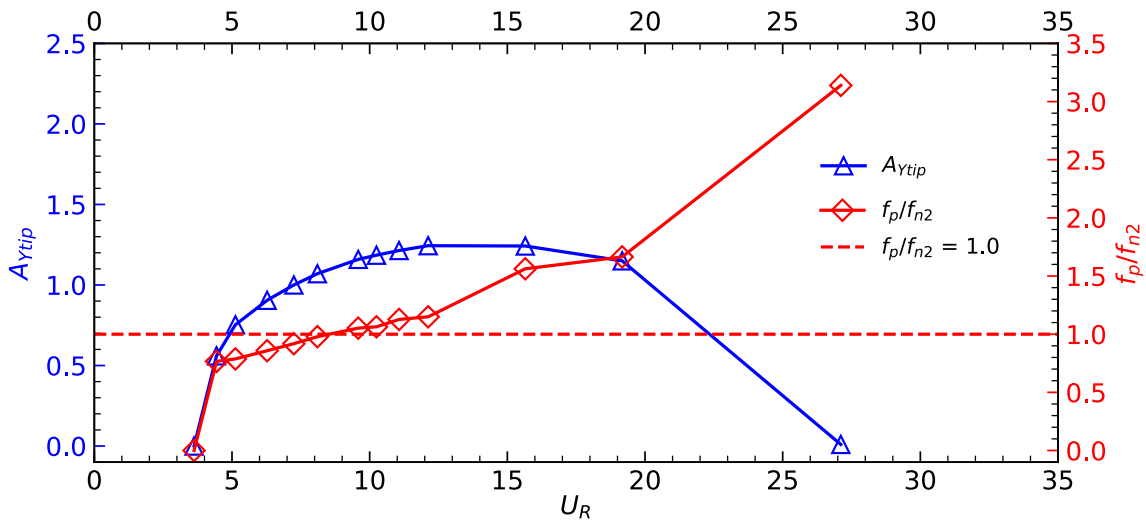


Fig. 12 Computed values of the plate amplitude (A_{Ytip}) as a function of reduced velocity (U_R). The bending stiffness (K_b) was varied and mass ratio is kept fixed at $M = 0.572$ for the cases plotted here.

Ratio of plate oscillation frequency and second-mode natural frequency of the plate in vacuum (f_p/f_{n2}) is plotted for all cases. A dotted line at $f_p/f_{n2} = 1.0$ is also shown

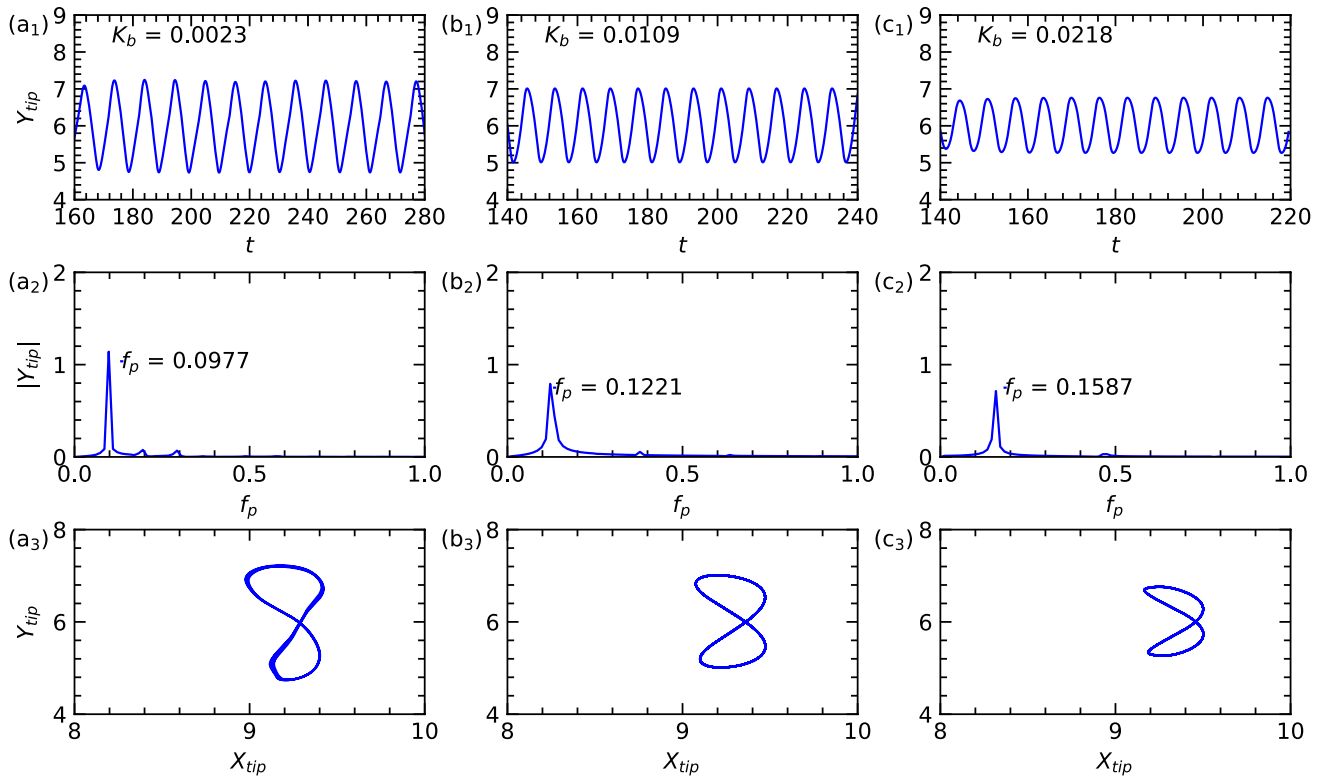


Fig. 13 Comparison of tip displacement Y_{tip} (first row), power spectra (second row), and phase-plane plots (third row) for three cases of bending stiffness, $K_b = 0.0023, 0.0109$ and 0.0218 , with same

mass ratio, $M = 0.572$. Phase-plane plots are shown after the plate amplitude reaches a plateau value

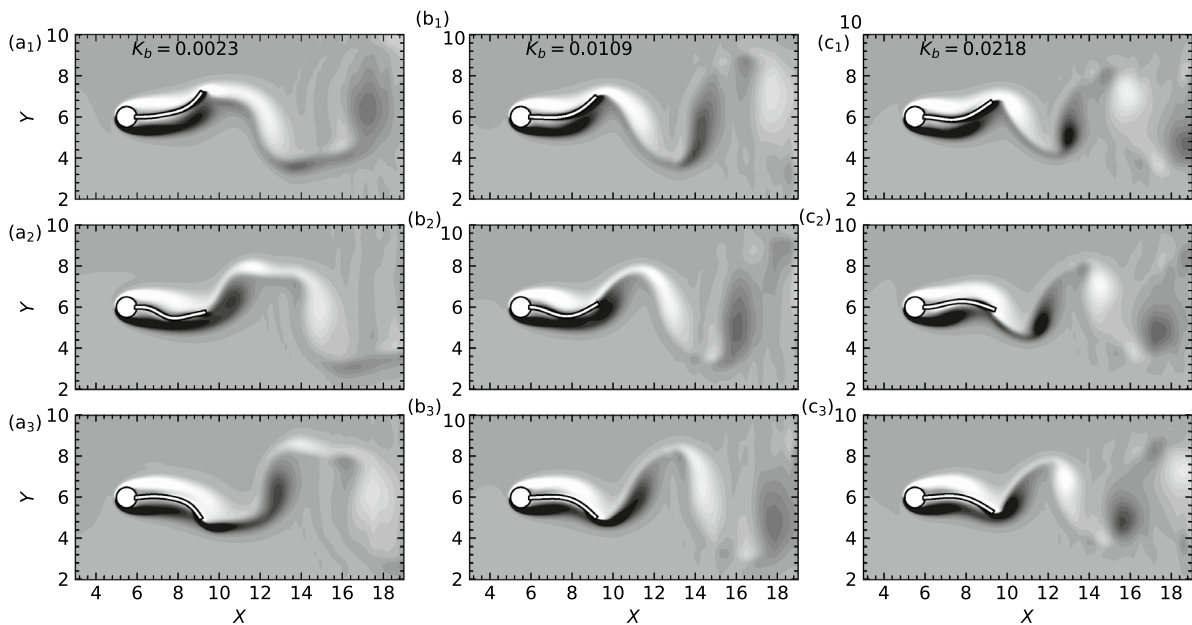


Fig. 14 Comparison of vorticity field at different time instances for three different values of bending stiffness, $K_b = 0.0023, 0.0109$ and 0.0218 , with the same mass ratio, $M = 0.572$. The color map range is $[-2, 2]$

Table 8 Recent previous studies which examined wind energy-based miniaturized energy harvesters

Study by	Mode of energy harvesting	Cantilever length/ cylinder diameter (l^* , mm)	Wind speed (m s^{-1})	Re based on l^*
Liu et al. [55]	FIV of a piezoelectric cantilever	3.0	3.9–15.6	760–3069
He et al. [56]	FIV of a piezoelectric cantilever with proof mass	3.0	0.6–16.3	1137–3175
Lee et al. [57]	VIV of a cylinder	2.0	1–6	130–779

The range of flow velocity and Re based on characteristic length in the study are listed in the table. Kinematic viscosity of air is taken as $1.54 \times 10^{-5} \text{ m}^2 \text{ s}^{-1}$ in ambient conditions for calculations of Re. In the present study, Re based on the plate length is 350

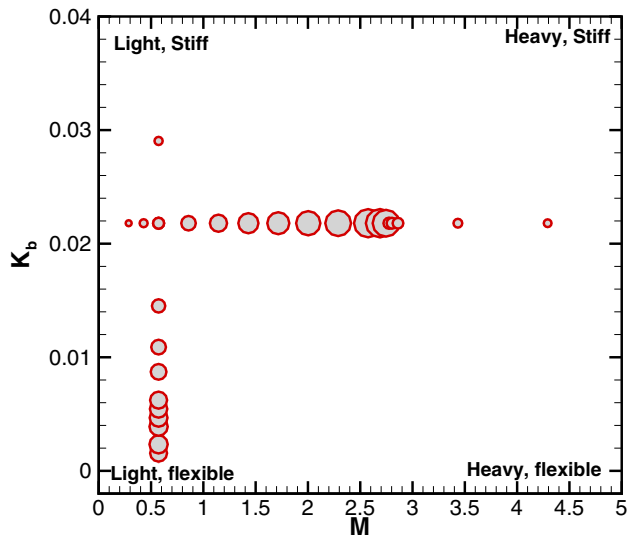


Fig. 15 Qualitative comparison of the amplitude of the plate tip on M – K_b plane for all cases. The radius of the circles are scaled with the magnitude of the computed amplitude. A large (small) M and K_b represent heavy (light) and stiff (flexible) plate, respectively

Acknowledgements R.B. gratefully acknowledges financial support from the Naval Research Board (NRB), New Delhi, India, through Grant NRB-403/-HYD/17-18. A.K. was a recipient of the Prime Minister Fellowship Scheme for Doctoral Research, a public–private partnership between Science and Engineering Research Board (SERB), and Confederation of Indian Industry (CII). The author's host institute for research was IITB-Monash Research Academy, and the partner company was Forbes Marshall Inc., Pune, India. We thank anonymous reviewers for their valuable suggestions.

Compliance with ethical standards

Conflict of interest The authors declare that they have no conflict of interest.

References

- Bhattacharya A, Shahajhan SSS (2016) Power extraction from vortex-induced angular oscillations of elliptical cylinder. *J Fluids Struct* 63:140–154
- Soti AK, Thompson MC, Sheridan J, Bhardwaj R (2017) Harnessing electrical power from vortex-induced vibration of a circular cylinder. *J Fluids Struct* 70:360–373
- Shoole K, Mittal R (2014) Computational study of flow-induced vibration of a reed in a channel and effect on convective heat transfer. *Phys Fluids* 26(12):127103
- Soti AK, Bhardwaj R, Sheridan J (2015) Flow-induced deformation of a flexible thin structure as manifestation of heat transfer enhancement. *Int J Heat Mass Transf* 84:1070–1081
- Joshi RU, Soti AK, Bhardwaj R (2015) Numerical study of heat transfer enhancement by deformable twin plates in laminar heated channel flow. *Comput Therm Sci Int J* 7(5–6):467–476
- Badhurshah R, Bhardwaj R, Bhattacharya A (2019) Lock-in regimes for vortex-induced vibrations of a cylinder attached to a bistable spring. *J Fluids Struct* 91:102697
- Mittal R, Iaccarino G (2005) Immersed boundary methods. *Ann Rev Fluid Mech* 37:239–261
- Sotiropoulos F, Yang X (2014) Immersed boundary methods for simulating fluidstructure interaction. *Prog Aerosp Sci* 65:1–21
- Bhardwaj R, Mittal R (2012) Benchmarking a coupled immersed-boundary-finite-element solver for large-scale flow-induced deformation. *AIAA J* 50:1638–1642
- Turek S, Hron J (2006) Proposal for numerical benchmarking of fluid-structure interaction between an elastic object and laminar incompressible flow. In: Bungartz H-J, Schäfer M (eds) *Fluid-structure interaction*. Springer, Berlin, pp 371–385
- Tian F-B, Dai H, Luo H, Doyle JF, Rousseau B (2014) Fluidstructure interaction involving large deformations: 3D simulations and applications to biological systems. *J Comput Phys* 258:451–469
- Bailoor S, Annangi A, Seo JH, Bhardwaj R (2017) Fluid-structure interaction solver for compressible flows with applications to blast loading on thin elastic structures. *Appl Math Model* 52:470–492
- Furquan M, Mittal S (2015) Flow past two square cylinders with flexible splitter plates. *Comput Mech* 55(6):1155–1166
- Küttler U, Wall WA, Ramm E (2008) Fixed-point fluid-structure interaction solvers with dynamic relaxation. *Comput Mech* 43:61–72
- Borazjani I, Ge L, Sotiropoulos F (2008) Curvilinear immersed boundary method for simulating fluid structure interaction with complex 3D rigid bodies. *J Comput Phys* 227(16):7587–7620
- Kim W, Lee I, Choi H (2018) A weak-coupling immersed boundary method for fluidstructure interaction with low density ratio of solid to fluid. *J Comput Phys* 359:296–311
- Degroote J, Haelterman R, Annereel S, Bruggeman P, Vierendeels J (2010) Performance of partitioned procedures in fluid-structure interaction. *Comput Struct* 88(7–8):446–457
- Vu HC, Ahn J, Hwang JH (2016) Numerical investigation of flow around circular cylinder with splitter plate. *KSCE J Civ Eng* 20:2559–2568

19. Sarioglu M (2017) Control of flow around a square cylinder at incidence by using a splitter plate. *Flow Meas Instrum* 53:221–229
20. Chauhan MK, Dutta S, More BS, Gandhi BK (2018) Experimental investigation of flow over a square cylinder with an attached splitter plate at intermediate Reynolds number. *J Fluids Struct* 76:319–335
21. Connell BS, Yue DK (2007) Flapping dynamics of a flag in a uniform stream. *J Fluid Mech* 581:33–67
22. Alben S (2015) Flag flutter in inviscid channel flow. *Phys Fluids* 27(3):033603
23. Akcabay DT, Young YL (2012) Hydroelastic response and energy harvesting potential of flexible piezoelectric beams in viscous flow. *Phys Fluids* 24(5):054106
24. Liu J, Jaiman RK, Gurugubelli PS (2014) A stable second-order scheme for fluid-structure interaction with strong added-mass effects. *J Comput Phys* 270:687–710
25. Tang L, Padoussis MP (2007) On the instability and the post-critical behaviour of two-dimensional cantilevered flexible plates in axial flow. *J Sound Vib* 305(1):97–115
26. Watanabe Y, Isogai K, Suzuki S, Sugihara M (2002) A theoretical study of paper flutter. *J Fluids Struct* 16(4):543–560
27. Argentina M, Mahadevan L (2005) Fluid-flow-induced flutter of a flag. *Proc Natl Acad Sci U S A* 102(6):1829–1834
28. Shelley MJ, Zhang J (2011) Flapping and bending bodies interacting with fluid flows. *Ann Rev Fluid Mech* 43:449–465
29. Lee JH, Huang W-X, Sung HJ (2014) Flapping dynamics of a flexible flag in a uniform flow. *Fluid Dyn Res* 46(5):055517
30. Alben S, Shelley MJ (2008) Flapping states of a flag in an inviscid fluid: bistability and the transition to chaos. *Phys Rev Lett* 100(7):074301
31. Eloy C, Souilliez C, Schouveiler L (2007) Flutter of a rectangular plate. *J Fluids Struct* 23(6):904–919
32. Eloy C, Lagrange R, Souilliez C, Schouveiler L (2008) Aeroelastic instability of cantilevered flexible plates in uniform flow. *J Fluid Mech* 611:97–106
33. Shoele K, Mittal R (2016) Flutter instability of a thin flexible plate in a channel. *J Fluid Mech* 786:29–46
34. Kundu A, Soti AK, Bhardwaj R, Thompson MC (2017) The response of an elastic splitter plate attached to a cylinder to laminar pulsatile flow. *J Fluids Struct* 68:423–443
35. Thomson W (1996) *Theory of vibration with applications*. CRC Press, Boca Raton ISBN 9780748743803
36. Shukla S, Govardhan R, Arakeri J (2013) Dynamics of a flexible splitter plate in the wake of a circular cylinder. *J Fluids Struct* 41:127–134
37. Sahu TR, Furquan M, Mittal S (2019) Numerical study of flow-induced vibration of a circular cylinder with attached flexible splitter plate at low Re. *J Fluid Mech* 880:551–593
38. Xu M, Wei M, Yang T, Lee YS (2016) An embedded boundary approach for the simulation of a flexible flapping wing at different density ratio. *Eur J Mech B/Fluids* 55:146–156
39. Mittal R, Dong H, Bozkurttas M, Najjar F, Vargas A, von Loebbecke A (2008) A versatile sharp interface immersed boundary method for incompressible flows with complex boundaries. *J Comput Phys* 227:4825–4852
40. Seo JH, Mittal R (2011) A sharp-interface immersed boundary method with improved mass conservation and reduced spurious pressure oscillations. *J Comput Phys* 230(19):7347–7363
41. Mittal R, Zheng X, Bhardwaj R, Seo JH, Xue Q, Bielamowicz S (2011) Toward a simulation-based tool for the treatment of vocal fold paralysis. *Front Physiol* 2:19
42. Soti AK (2018) *Computational and experimental investigation of fluid-structure interaction with applications in energy harvesting and thermal augmentation*. Ph.D. dissertation, IITB-Monash Research Academy, Indian Institute of Technology Bombay, Mumbai
43. Kundu A (2019) *Computational study of interaction of an elastic plate with laminar flow involving large-scale flow-induced deformation*. Ph.D. dissertation, IITB-Monash Research Academy, Indian Institute of Technology Bombay, Mumbai
44. Bhardwaj R, Ziegler K, Seo JH, Ramesh KT, Nguyen TD (2014) A computational model of blast loading on the human eye. *Bio-mech Model Mechanobiol* 13(1):123–140
45. Garg H, Soti AK, Bhardwaj R (2018) A sharp interface immersed boundary method for vortex-induced vibration in the presence of thermal buoyancy. *Phys Fluids* 30(2):023603
46. Mishra R, Kulkarni SS, Bhardwaj R, Thompson MC (2019) Response of a linear viscoelastic splitter plate attached to a cylinder in laminar flow. *J Fluids Struct* 87:284–301
47. Wall WA, Ramm E (1998) Fluid structure interaction based upon a stabilized (ALE) finite element method. In: SFB 404, Geschäftsstelle
48. Olivier M, Dumas G, Morissette J (2009) A fluid-structure interaction solver for nano-air-vehicle flapping wings. In: *Proceedings of the 19th AIAA computational fluid dynamics conference*, San Antonio, USA, pp 1–15
49. Habchi C, Russeil S, Bougeard D, Harion J-L, Lemenand T, Ghanem A, Della Valle D, Peerhossaini H (2013) Partitioned solver for strongly coupled fluid-structure interaction. *Comput Fluids* 71:306–319
50. Williamson CH, Govardhan R (2004) Vortex-induced vibrations. *Ann Rev Fluid Mech* 36:413–455
51. Khalak A, Williamson C (1997) Fluid forces and dynamics of a hydroelastic structure with very low mass and damping. *J Fluids Struct* 11(8):973–982
52. Khalak A, Williamson C (1999) Motions, forces and mode transitions in vortex-induced vibrations at low mass-damping. *J Fluids Struct* 13(7–8):813–851
53. Govardhan R, Williamson C (2000) Modes of vortex formation and frequency response of a freely vibrating cylinder. *J Fluid Mech* 420:85–130
54. Park JW, Cho S, Jung H-J, Yun C-B, Jang SA, Jo H, Spencer BF, Nagayama T, Seo J-W (2010) Long-term structural health monitoring system of a cable-stayed bridge based on wireless smart sensor networks and energy harvesting techniques. In: *5th World conference on structural control and monitoring*, pp 1–6
55. Liu H, Zhang S, Kathiresan R, Kobayashi T, Lee C (2012) Development of piezoelectric microcantilever flow sensor with wind-driven energy harvesting capability. *Appl Phys Lett* 100(22):223905
56. He X, Shang Z, Cheng Y, Zhu Y (2013) A micromachined low-frequency piezoelectric harvester for vibration and wind energy scavenging. *J Micromech Microeng* 23(12):125009
57. Lee YJ, Qi Y, Zhou G, Lua KB (2019) Vortex-induced vibration wind energy harvesting by piezoelectric MeMS device in formation. *Sci Rep* 9(1):1–11

Publisher's Note Springer Nature remains neutral with regard to jurisdictional claims in published maps and institutional affiliations.